

# Backbone Dynamics of the 18.5 kDa Isoform of Myelin Basic Protein Reveals Transient $\alpha$ -Helices and a Calmodulin-Binding Site

David S. Libich and George Harauz

Department of Molecular and Cellular Biology, and Biophysics Interdepartmental Group, University of Guelph, Guelph, Ontario, Canada

**ABSTRACT** The 18.5 kDa isoform of myelin basic protein (MBP) is the predominant form in adult human central nervous system myelin. It is an intrinsically disordered protein that functions both in membrane adhesion, and as a linker connecting the oligodendrocyte membrane to the underlying cytoskeleton; its specific interactions with calmodulin and SH3-domain containing proteins suggest further multifunctionality in signaling. Here, we have used multidimensional heteronuclear nuclear magnetic resonance spectroscopy to study the conformational dependence on environment of the protein in aqueous solution (100 mM KCl) and in a membrane-mimetic solvent (30% TFE- $d_2$ ), particularly to analyze its secondary structure using chemical shift indexing, and to investigate its backbone dynamics using  $^{15}\text{N}$  spin relaxation measurements. Collectively, the data revealed three major segments of the protein with a propensity toward  $\alpha$ -helicity that was stabilized by membrane-mimetic conditions: T33-D46, V83-T92, and T142-L154 (murine 18.5 kDa sequence numbering). All of these regions corresponded with bioinformatics predictions of ordered secondary structure. The V83-T92 region comprises a primary immunodominant epitope that had previously been shown by site-directed spin labeling and electron paramagnetic resonance spectroscopy to be  $\alpha$ -helical in membrane-reconstituted systems. The T142-L154 segment overlapped with a predicted calmodulin-binding site. Chemical shift perturbation experiments using labeled MBP and unlabeled calmodulin demonstrated a dramatic conformational change in MBP upon association of the two proteins, and were consistent with the C-terminal segment of MBP being the primary binding site for calmodulin.

## INTRODUCTION

The genes of the oligodendrocyte lineage (Golli) produce several isoforms of the myelin basic protein (MBP) family, arising from three transcription start sites and differential exon splicing (1,2). The classic isoforms of MBP arise from transcription start site 3, and are expressed primarily in the mature central nervous system, where they are known to maintain the compaction of the myelin sheath (3). It has been suggested that some variants of MBP might have further roles in myelin signaling and cytoskeletal assembly (3–7), because of their myriad combinatorial posttranslational modifications (phosphorylation, methylation, deimination) (7,8), specific binding to  $\text{Ca}^{2+}$ -calmodulin (9–11) and SH3-domains (12), and ability to polymerize and bundle actin and tubulin (13–17). Myelin basic protein is implicated in the pathogenesis of the neurodegenerative disease multiple sclerosis as a mediator of myelin degeneration due to increased deimination, and as a candidate self-antigen (8,18–21).

Based on their net charge to mean hydrophobicity ratio, and various spectroscopic measurements, all known forms of MBP (both classic and Golli) belong to the class of intrinsically disordered proteins (IDPs), sometimes also called intrinsically unstructured proteins (7,22–24). Many IDPs are multifunctional and/or involved in signaling pathways (25–27). They have an extended conformation to present a large

effective surface area for interaction with a variety of diverse ligands, which they bind with high specificity, and are often hubs (or central linkers) of protein interaction networks (28–31). These intermolecular associations may involve preformed (inherent and transient, or induced) structural elements such as  $\alpha$ -helices, and/or an induced fit, i.e., coupled folding and binding (32–44). Dunker and colleagues have encapsulated this idea in their molecular recognition fragments (MoRF, specifically  $\alpha$ -MoRF) hypothesis (45,46).

The most powerful approach to probing the conformational dynamics and interactions of IDPs is nuclear magnetic resonance (NMR) spectroscopy (47–52). Since the propensity of IDPs to adopt different conformations is highly dependent on their environment and on their binding partners, comparative NMR studies of MBP under differing conditions will provide important insights into the structural and functional details of this family (7). A peptide fragment encompassing an immunodominant epitope of MBP (corresponding to murine 18.5 kDa residues P82–P93) has been characterized by solution NMR in aqueous buffer, in 30% trifluoroethanol (TFE- $d_2$ , a membrane-mimetic solvent ( $\text{CF}_3\text{-CD}_2\text{-OH}$ )), and in deuterated dodecylphosphocholine (DPC- $d_{38}$ ) micelles (53). In the whole protein, this segment of MBP had previously been shown by site-directed spin-labeling (SDSL) and electron paramagnetic resonance (EPR) spectroscopy to be an amphipathic  $\alpha$ -helix lying on the surface of the myelin membrane, slightly tilted and partially embedded (54). The structure of the fragment studied by solution NMR was, indeed,  $\alpha$ -helical in TFE- $d_2$  and in the DPC- $d_{38}$  micelles.

Submitted November 16, 2007, and accepted for publication February 8, 2008.

Address reprint requests to George Harauz, Tel.: 519-824-4120, x52535; E-mail: gharauz@uoguelph.ca.

Editor: Kathleen B. Hall.

© 2008 by the Biophysical Society  
0006-3495/08/06/4847/20 \$2.00

doi: 10.1529/biophysj.107.125823

We have performed multidimensional heteronuclear solution NMR and backbone assignment of full-length 18.5 kDa recombinant murine MBP (rmMBP, a posttranslationally unmodified form of 176 residues) in both 30% TFE- $d_2$  (55), and in 100 mM KCl solution (56). In this study, multidimensional heteronuclear NMR spectroscopy was used to probe further the structure and dynamics of rmMBP under these two different solution conditions. The deviation of chemical shifts of many spins (including  $^{13}C^\alpha$ ,  $^{13}C^\beta$ , and  $^1H^\alpha$ ) from random coil values provides a sensitive probe of secondary structure propensities (57–59). The measurement of  $^{15}N$  and spin relaxation rates provides information about internal dynamics of proteins on the picosecond-to-nanosecond and microsecond-to-millisecond timescales (47,60,61). Here, we have identified several segments of rmMBP that form transient  $\alpha$ -helices, representing putative binding targets for other proteins. One of these segments has been strongly implicated as being the primary binding site for calmodulin, identified using chemical shift perturbation analysis. This result adds to the mounting evidence that the physiological role of MBP in central nervous system myelin is more than simply a membrane adhesion factor, but that it is, in fact, a multifunctional adaptor protein (3,9,11,12,14,15).

## MATERIALS AND METHODS

### Materials

Most chemicals were reagent grade and acquired from either Fisher Scientific (Unionville, ON, Canada) or Sigma-Aldrich (Oakville, ON, Canada). Electrophoresis grade chemicals were purchased from ICN Biomedicals (Costa Mesa, CA) or Bio-Rad Laboratories (Mississauga, ON, Canada). The nitrilotriacetic-acid agarose beads were purchased from Qiagen (Mississauga, ON, Canada). The stable isotopic compounds  $D_2O$ ,  $^{15}NH_4Cl$ , and  $^{13}C_6$ -glucose were obtained from Cambridge Isotope Laboratories (Andover, MA).

### Protein expression and purification

Uniformly  $^{15}N$ - or  $^{13}C^{15}N$ -labeled recombinant murine MBP (rmMBP, 176 residues including an LEH<sub>6</sub> tag) was expressed in *Escherichia coli* BL21-CodonPlus(DE3)-RP cells (Stratagene, La Jolla, CA), grown in M9 minimal media with either  $^{15}NH_4Cl$  and/or  $^{13}C_6$ -glucose (Cambridge Isotope Laboratories) as the sole nitrogen and/or carbon source(s). Purification was as previously described (62) with minor modifications to improve recovery (55,56). A yield of ~10–12 mg of purified, labeled rmMBP was obtained per liter of culture.

The plasmid-encoding *Xenopus laevis* calmodulin with a hexahistidine tag (pET-3a-CaM) was a generous gift from Dr. Mitsuru Ikura (Ontario Cancer Institute, Toronto, ON, Canada). Uniformly  $^{15}N$ -labeled *X. laevis* calmodulin (CaM) was prepared as previously described (63), with a yield of ~40 mg of protein per liter of culture.

Protein concentrations were determined here by measuring the absorbance at 280 nm, a parameter that we have calibrated by amino-acid analysis. The values of the extinction coefficients used were 0.623 L g<sup>-1</sup> cm<sup>-1</sup> (rmMBP), and 0.152 L g<sup>-1</sup> cm<sup>-1</sup> (CaM). These values (in 6.0 M guanidine hydrochloride, 0.02 M phosphate, pH 6.5), were calculated on the basis of

the amino-acid sequences using the ProtParam software tool (available at <http://www.expasy.ch>).

### Solution NMR spectroscopy

Backbone and most side-chain resonance assignments for uniformly  $^{13}C^{15}N$ -labeled rmMBP dissolved in either 30% TFE- $d_2$ , or in 100 mM KCl, have been previously reported. In these first studies, complementary three-dimensional heteronuclear NMR experiments for establishing backbone connectivity were performed at either 300 K (2 mM  $^{13}C^{15}N$ -rmMBP in 30% TFE- $d_2$ , pH 6.5) (55), or at 277 K (2 mM  $^{13}C^{15}N$ -rmMBP in 100 mM KCl, pH 6.5, 10%  $D_2O$ ) (56). Here, new backbone resonance assignments for 18.5 kDa rmMBP in 100 mM KCl at 300 K were obtained by tracking the gradual shift of observable crosspeaks in a series of heteronuclear single quantum coherence (HSQC) experiments recorded at 277 K, 283 K, 289 K, 295 K, and 300 K. The temperature series was recorded on an Avance spectrometer (Bruker BioSpin, Milton, Ontario, Canada) operating at a proton Larmor frequency of 600.13 MHz, using identical acquisition and processing parameters to those previously reported (56,64). These additional resonance assignments were deposited, as an addendum, to the Biological Magnetic Resonance Databank (BMRB) with accession number 15131.

### Secondary chemical shifts

The chemical shift deviations from random coil values were used to assess the secondary structure propensities along the backbone of rmMBP. Random coil values (65) were corrected for sequence dependence using sequence-specific correction factors determined for a set of Ac-GGXGG-NH<sub>2</sub> peptides in 8 M urea at pH 2.3 (66). The normalized sequence-corrected chemical shift indices  $\Delta\delta C^\alpha$ ,  $\Delta\delta C^\beta$ ,  $\Delta\delta N$ , and  $\Delta\delta H^N$ , for  $C^\alpha$ ,  $C^\beta$ , N, and  $H^N$ , respectively, were combined to yield a normalized chemical shift index (CSI):

$$CSI_{\text{norm}} = 1/2 ([\Delta\delta C^\alpha]_{\text{norm}} - 1/3([\Delta\delta C^\beta]_{\text{norm}} + [\Delta\delta N]_{\text{norm}} + [\Delta\delta H^N]_{\text{norm}})). \quad (1)$$

The chemical shift indices were calculated using an in-house script as previously performed (64), written in Lua (Pontifical Catholic University of Rio de Janeiro, Brazil) and executed in computer-aided resonance assignment (CARA) 1.8.3 (67). The  $C^\alpha$ ,  $C^\beta$ , and  $H^\alpha$  chemical shift data were also used to assess the secondary structure propensity of rmMBP using the program SSP (68).

### $^{15}N$ relaxation measurements

All relaxation experiments were recorded on uniformly  $^{15}N$ -labeled MBP samples (1.72 mM  $^{15}N$ -rmMBP in 30% TFE- $d_2$ , pH 6.5, 1 mg 2,2-dimethyl-2-silapentane-5-sulfonic acid (DSS); or 1.75 mM  $^{15}N$ -rmMBP in 100 mM KCl, pH 6.5, 10%  $D_2O$ , 1 mg DSS). The relaxation parameters of  $^{15}N$  were measured using standard approaches (69–71). The spin-lattice  $R_1$  rate measurements were conducted with relaxation delays of 1.6, 50, 100, 200, 300, 400, 800, 1000, and 1200 ms as previously described (70,71). The spin-spin relaxation constant  $R_2$  measurements were done with Carr-Purcell-Meiboom-Gill (72) delays of 0, 64, 128, 160, 192, 224, 256, 288, and 320 ms. The relaxation rates for both  $R_1$  and  $R_2$  were determined from the decay of the intensity of each  $^1H$ - $^{15}N$  crosspeak in this series of spectra. All of the relaxation parameters, along with the  $\{^1H\}$ - $^{15}N$  nuclear Overhauser effect (NOE) intensities for backbone  $^{15}N$  nuclei, were measured at 300 K, at a magnetic field strength of 14.1 T (corresponding to the resonance frequency of 600.13 MHz for  $^1H$ ), and sweep widths of 12 parts per million (ppm) ( $^1H$ ) and 35 ppm ( $^{15}N$ ). The number of points was 256 and 2048 in the indirect and direct dimensions, respectively, with 48 transients per point.

The relaxation constants and the experimental errors were extracted by a single exponential curve-fitting of the peak heights using a SPARKY (T. D. Goddard and D. G. Kneller, SPARKY 3, University of California, San Francisco) built-in option. The best fit was obtained by minimizing the root mean-square deviation of the experimental peak heights from the fit. Random errors for  $R_1$  and  $R_2$  values were estimated by calculating a best fit for a set of perturbed heights 5000 times; the heights were perturbed by computer-simulated noise with a Gaussian distribution of zero mean, and with variance equal to the root mean-square deviation of the heights from the original best fit. The spread in the best-fit values was used as a measure of the experimental random error.

The steady-state  $\{^1\text{H}\}$ - $^{15}\text{N}$  NOE intensities were obtained from the ratio  $I_{\text{NOE}}/I_{\text{NONOE}}$ , where  $I_{\text{NOE}}$  and  $I_{\text{NONOE}}$  are the peak heights in the NOE spectra with and without proton saturation, respectively. These spectra were collected using a standard experiment (70), with the same acquisition parameters as those of the HSQC spectrum, except that the number of transients per point was 192. The uncertainty in measuring NOE intensities was determined as previously described (64,73).

## Spectral density function

The frequency components of the relaxation parameters  $R_1$ ,  $R_2$ , and NOE are described by the spectral density function  $J(\omega)$  (73,74). Here,

$$R_1 = (d^2/4)[J(\omega_{\text{H}} - \omega_{\text{N}}) + 3J(\omega_{\text{N}}) + 6J(\omega_{\text{H}} + \omega_{\text{N}})] + c^2J(\omega_{\text{N}}), \quad (2)$$

$$R_2 = (d^2/8)[4J(0) + J(\omega_{\text{H}} - \omega_{\text{N}}) + 3J(\omega_{\text{N}}) + 6J(\omega_{\text{H}}) + 6J(\omega_{\text{H}} + \omega_{\text{N}})] + (c^2/6)[4J(0) + 3J(\omega_{\text{N}})] + R_{\text{ex}}, \quad (3)$$

$$\text{NOE} = 1 + (d^2/4R_1)(\gamma_{\text{N}}/\gamma_{\text{H}})[6J(\omega_{\text{H}} + \omega_{\text{N}}) - J(\omega_{\text{H}} - \omega_{\text{N}})], \quad (4)$$

where  $d = (\mu_0 h \gamma_{\text{N}} \gamma_{\text{H}} / 8\pi^2) \langle r_{\text{NH}}^{-3} \rangle$ ,  $c = \omega_{\text{N}} \Delta\sigma / \sqrt{3}$ ,  $\mu_0$  is the permeability of free space,  $h$  is Planck's constant,  $\gamma_{\text{H}}$  and  $\gamma_{\text{N}}$  are gyromagnetic ratios of hydrogen and nitrogen nuclei, respectively,  $r_{\text{NH}}$  is the proton-nitrogen bond length,  $\omega_{\text{H}}$  and  $\omega_{\text{N}}$  are the Larmor frequencies for proton and nitrogen, respectively, and  $\Delta\sigma$  is the chemical shift anisotropy of  $^{15}\text{N}$  ( $-160$  ppm). Here,  $R_{\text{ex}}$  is a term introduced to account for contributions arising from conformational averaging on the microsecond-to-millisecond timescale that are not averaged by the Carr-Purcell-Meiboom-Gill (72) pulse train.

The three experimental parameters  $R_1$ ,  $R_2$ , and NOE are not sufficient to extract the spectral density function  $J(\omega)$  at five frequencies. However, the values of  $J(\omega_{\text{H}})$ ,  $J(\omega_{\text{H}} + \omega_{\text{N}})$ , and  $J(\omega_{\text{H}} - \omega_{\text{N}})$  can be assumed to be approximately equal in the case of  $^{15}\text{N}$  relaxation (75). Furthermore, if the contribution from slow conformational exchange,  $R_{\text{ex}}$ , is assumed to be negligible compared to the other terms under certain conditions, then Eqs. 2–4 can be solved to calculate the spectral density function at three frequencies:

$$J(\omega_{\text{H}}) = 0.2R_1(\text{NOE} - 1)(4/d^2)(\gamma_{\text{N}}/\gamma_{\text{H}}), \quad (5)$$

$$J(\omega_{\text{N}}) = 4R_1/(3d^2 + 4c^2)[1 - (7/5)(\text{NOE} - 1)(\gamma_{\text{N}}/\gamma_{\text{H}})], \quad (6)$$

$$J(0) = 1/(3d^2 + 4c^2)[6R_2 - 3R_1 - (18R_1/5)(\text{NOE} - 1)(\gamma_{\text{N}}/\gamma_{\text{H}})]. \quad (7)$$

The  $R_1$ ,  $R_2$ , and NOE values measured at 300 K, and the  $^1\text{H}$  frequency of 600.13 MHz were used as input parameters for Eqs. 5–7. The uncertainties of these inputs were combined using the standard error propagation methods to propagate the uncertainties in the calculated spectral density values, as was previously performed for the Golli-MBP isoform rmBG21 (64,73).

## Model-free analysis

To quantify further the microscopic local motion parameters of the amide  $^{15}\text{N}$  relaxation rates, a Lipari-Szabo (76,77) analysis with the extension of Clore et al. (78), was performed with the MODELFREE (v. 4.20) software suite (79,80). In this treatment, the spectral density function is assumed to be related to a set of internal motional parameters which include descriptions of the correlation times ( $\tau_{\text{m}}$ ,  $\tau_{\text{s}}$ , and  $\tau_{\text{f}}$ ) and order parameters ( $S^2$ ,  $S_{\text{s}}^2$ , and  $S_{\text{f}}^2$ ). The fast and slow internal correlation times are given by  $\tau_{\text{f}}$  and  $\tau_{\text{s}}$ , respectively, whereas the overall correlation time of the molecule is  $\tau_{\text{m}}$ . Likewise,  $S_{\text{s}}^2$ ,  $S_{\text{f}}^2$ , and  $S^2 = S_{\text{s}}^2 S_{\text{f}}^2$ , are the descriptions of the slow, fast, and generalized motions, respectively.

The initial estimates for  $\tau_{\text{m}}$  for rmMBP in either 30% TFE- $\text{d}_2$  or 100 mM KCl were obtained using the MODELFREE grid search function. The models that describe the local motions of the individual NH vectors were optimized separately according to the procedure outlined by Mandel et al. (79). This strategy accounts for the different timescales of the motions arising from structural variations, motional restrictions, and/or exchange. A summary of the models used for 18.5 kDa rmMBP is given in Supplementary Material, Data S1, Table S1. Different rotational diffusion models included in the MODELFREE software package were evaluated, and the isotropic diffusion model was found to provide the best fit to the rmMBP relaxation data for both experimental conditions examined (30% TFE- $\text{d}_2$ , 100 mM KCl). For the final model fitting, a maximum of three rotational parameters and the overall correlation time could be fit to  $R_1$ ,  $R_2$ , and NOE acquired at 600 MHz. Errors were determined based on 500 Monte Carlo simulations of Brent's implementation of Powell's method for multidimensional minimization (MODELFREE manual (80)).

## Interactions with $\text{Ca}^{2+}$ -calmodulin

Samples of rmMBP with CaM were prepared where only one of the binding partners was isotopically labeled, and the unlabeled partner was in molar excess. A series of combinations was prepared which allowed for the assessment of structural changes in both binding partners based on chemical shift perturbations. The following samples were prepared to examine rmMBP-CaM binding: 1), 0.9 mM  $^{15}\text{N}$ -rmMBP; 2), 1.25 mM  $^{15}\text{N}$ -CaM; 3), 0.78 mM  $^{13}\text{C}^{15}\text{N}$ -rmMBP with 0.96 mM CaM; and 4), 0.80 mM rmMBP with 0.64 mM  $^{15}\text{N}$ -CaM. All proteins were dissolved in 100 mM KCl, 8 mM  $\text{CaCl}_2$ , pH 6.5, 10%  $\text{D}_2\text{O}$ , with 0.75 mg DSS added as an internal reference. Briefly, rmMBP and CaM were first dissolved separately in distilled, de-ionized water at concentrations  $<1$  mg/mL; the samples were exchanged to the experimental buffer using Amicon Ultra 10,000 MWCO spin filters (Millipore, Billerica, MA). Calmodulin was slowly titrated into the rmMBP solution and concentrated using the same spin filter. The final volume was reduced to 500  $\mu\text{L}$ , and the samples were introduced into  $\text{D}_2\text{O}$ -matched Shigemi NMR tubes (Shigemi, Allison Park, PA).

The  $^1\text{H}$ - $^{15}\text{N}$  HSQCs were recorded for each sample on an Avance III spectrometer (Bruker) operating at a proton Larmor frequency of 800.23 MHz. Sequential backbone assignments of  $^{13}\text{C}^{15}\text{N}$ -rmMBP (sample 3, above) were accomplished using the Bruker suite of standard three-dimensional heteronuclear experiments: CBCA(CO)NH, CBCANH, and HCC(CO)NH (81). All three-dimensional spectra were acquired using 12 transients,  $2048 \times 40 \times 128$  ( $F_3 \times F_2 \times F_1$ ) points employing echo-anti-echo ( $F_2$ ) (82) and states-time-proportional phase incrementation quadrature ( $F_1$ ) detection. The sweep widths were 12, 32, and 83 ppm with the carrier frequencies set at 4.7, 119, and 39 ppm for  $F_3$ ,  $F_2$ , and  $F_1$ , respectively. The spectra were apodized using a shifted ( $\pi/3$ ), squared, sinusoidal bell function, zero-filled, and linear-predicted (forward with 8 ( $F_2$ ) and 16 ( $F_1$ ) prediction coefficients) before Fourier transformation. The software package TopSpin 2.0 (Bruker BioSpin, Rheinstetten, Germany) was used for spectral processing. The  $^1\text{H}$  chemical shifts were referenced to the internal methyl signal of DSS. The  $^{15}\text{N}$  and  $^{13}\text{C}$  chemical shifts were indirectly referenced using IUPAC recommended ratios of 0.251449530 ( $\gamma^{13}\text{C}/\gamma^1\text{H}$ ) and 0.101329118 ( $\gamma^{15}\text{N}/\gamma^1\text{H}$ ) (82). Assignments were done using CARA 1.8.3 (67), and modules contained in the CARA software package (<http://www.nmr.ch>).

## RESULTS AND DISCUSSION

### Chemical shift assignment of full-length 18.5 kDa rmMBP under different conditions

We initially performed multidimensional heteronuclear solution NMR studies of 18.5 kDa rmMBP in 30% TFE- $d_2$  (55) (BMRB accession number 6100). These conditions were chosen to mimic the membrane environment of the myelin sheath, while keeping the system experimentally tractable to solution NMR methodology (7). We argue that 30% TFE stabilizes transient  $\alpha$ -helices within the protein (83–85) on the basis of multiple, complementary studies on the immunodominant epitope of MBP (murine residues P82-P93). This segment forms an amphipathic, membrane surface-associated  $\alpha$ -helix in full-length rmMBP reconstituted with myelin-lipid vesicles (54,86). Solution NMR studies of an 18-residue peptide encompassing this fragment showed this epitope to be disordered in aqueous solution, and  $\alpha$ -helical in both 30% TFE- $d_2$  and DPC- $d_{38}$  micelles (53). Since the TFE solution condition stabilized this real  $\alpha$ -helix, we consider that other  $\alpha$ -helical segments identified in MBP under these conditions are also likely to be functionally relevant, considering the multitude of interaction partners already identified for this protein (7).

We acknowledge that results obtained with TFE and other fluorinated alcohols should always be interpreted with caution (83,85,87). Most importantly, however, membrane-mimetic conditions using organic solvents are unsuitable to probe interactions of MBP with proteins such as  $Ca^{2+}$ -CaM (9), due to the potential (and uncharacterized) influence of the solvent on the function of calmodulin (D. S. Libich, V. V. Bamm, and G. Harauz, unpublished data). Therefore, these studies were more recently extended to rmMBP in 100 mM KCl solution, a more physiologically relevant condition that emulates the intracellular cytosolic oligodendrocyte environment (56) (BMRB accession number 15131), and in which the structure of  $Ca^{2+}$ -CaM has been extensively characterized (88).

Although a peptide fragment (residues Q78-T95) of rmMBP has also been studied in DPC- $d_{38}$  micelles (53), the NMR spectra of the full-length protein under these conditions showed considerable peak broadening (results not shown). Since one of the main functions of 18.5 kDa MBP is membrane adhesion, it aggregates lipid vesicles in vitro (89). Thus, reconstituting full-length 18.5 kDa MBP with lipid micelles or vesicles results in excessively large complexes or aggregates, so that obtaining usable data under these conditions is impossible using solution NMR methodologies. Such reconstituted systems are better suited for solid-state NMR studies. An approach using several complementary heteronuclear correlation experiments to achieve a partial assignment of the mobile fragments of membrane-associated MBP has recently been described (90). However, solid-state NMR requires considerable further development before a full three-dimensional structure can be realized, particularly to probe

the membrane-embedded segments (91). Here, solution NMR was applied to study aspects of 18.5 kDa MBP's multifunctionality by focusing on the two conditions under which resonance assignments could be achieved, an aqueous and a membrane-mimetic environment.

The  $^1H$ - $^{15}N$  HSQC spectrum of full-length 18.5 kDa rmMBP in 100 mM KCl at 300 K is shown in Fig. 1, for comparison with previously published HSQCs of the protein in 30% TFE- $d_2$  at 298 K (55), and in 100 mM KCl at 277 K (56). The new assignments in Fig. 1 were obtained by tracking the crosspeaks assigned at 277 K through a series of temperature-dependent spectra, and have been deposited in the BMRB under accession number 15131. The absence of significant protein aggregation in these preparations is supported by previous fluorescence spectroscopy and dynamic light scattering experiments (9), as well as the relative quality and reproducibility of the HSQC spectra (55,56).

### Chemical shift index analysis

Chemical shift index (CSI) analysis can be used to assess the occurrence, proportion, and type of ordered secondary structure ( $\alpha$ -helix,  $\beta$ -strand) in a protein under different conditions (57–59). A more detailed analysis of the chemical shift data, which accounts for the probability that a particular sequence of residues will occupy structured space, can be obtained using the secondary structure propensity (SSP) algorithm (68). Chemical shift difference plots for rmMBP in 30% TFE- $d_2$ , the solution membrane-mimetic condition, are given in Fig. 2. The corresponding chemical shift data for the protein in 100 mM KCl are given in [Data S1](#), Fig. S1. The normalized CSI and SSP values are presented in Fig. 3 for the protein dissolved in 30% TFE- $d_2$  (Fig. 3, *A* and *B*), and in 100 mM KCl (Fig. 3, *C* and *D*). These experimental data are presented for comparison with a theoretical prediction of intrinsic disorder using Predictor of Naturally Disordered Regions (PONDR) (92,93) (Fig. 3 *E*), a secondary structure prediction using Garnier-Osguthorpe-Osborne (GOR) 4 (94) (Fig. 3 *F*), and hydrophobic cluster analysis (HCA) (95) (Fig. 3 *G*).

The chemical shifts of full-length rmMBP dissolved in 100 mM KCl are considerably different from those obtained for the protein under solution membrane-mimetic conditions, i.e., 30% TFE- $d_2$ , as previously observed with an 18-residue peptide fragment (53). CSI analysis confirmed some expected environment-specific structural details. Notably, the amphipathic  $\alpha$ -helix (P82-P93) present in the full-length protein in membrane-associated form (54,86), or in an 18-residue MBP-derived peptide under solution membrane-mimetic conditions (53), appears disordered here under aqueous conditions. SSP analysis indicates that the same regions of 18.5 kDa rmMBP are capable of forming  $\alpha$ -helices in both TFE and KCl (Fig. 3, *A* and *C*, respectively) The CSI analysis clearly shows the formation of stable  $\alpha$ -helices in several distinct regions of rmMBP in 30% TFE- $d_2$  (Fig. 3 *B*), but not in 100 mM KCl (Fig. 3 *D*). These measurements of secondary

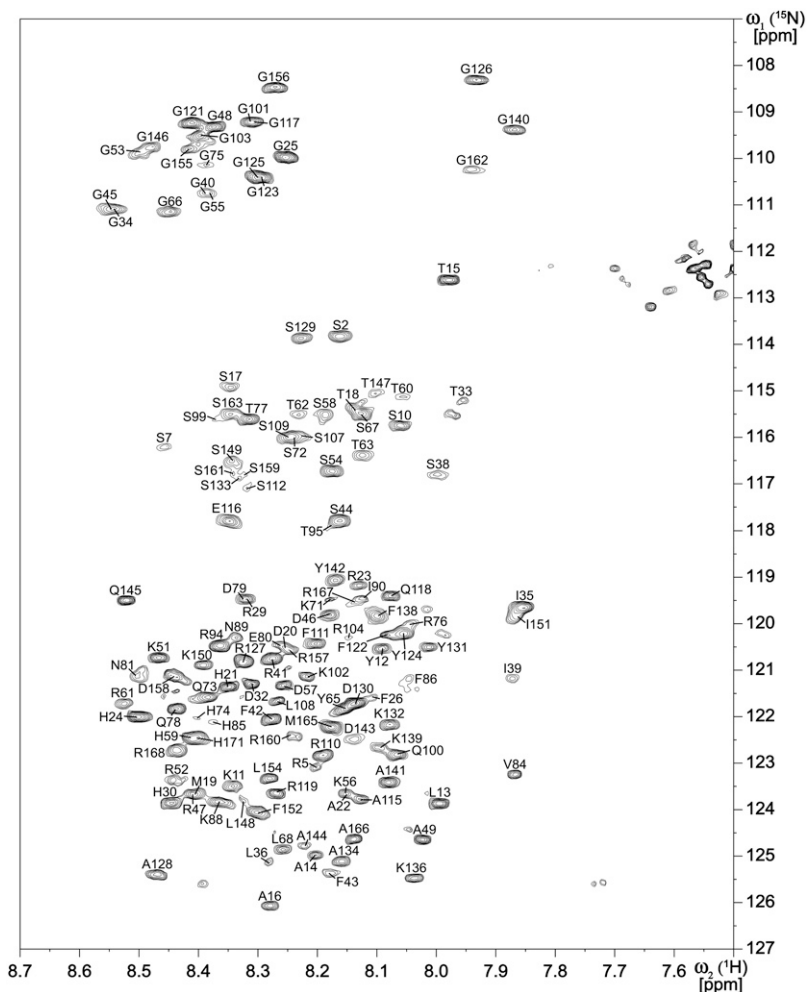


FIGURE 1 The  $^1\text{H}$ - $^{15}\text{N}$  HSQC spectrum of uniformly  $^{15}\text{N}$ -labeled rmMBP (176 residues, including a C-terminal LEH<sub>6</sub> tag) dissolved in 100 mM KCl in water at a concentration of 1.75 mM, recorded at 300 K. A total of 160 of 164 expected backbone peaks are assigned (there are 11 prolyl residues); peaks that appear below the displayed contour levels are not shown. Assignments are based on the assignments first performed at 277 K (56), and were obtained by tracking the assigned crosspeaks through a series of spectra recorded at increasingly higher temperatures.

structure correspond to the regions of order predicted by PONDR (Fig. 3 E). Here, there are three sections of MBP that form  $\alpha$ -helices in the membrane-mimetic solvent, and that correspond to the CSI, SSP, and HCA predictions: T33-D46, V83-T92, and T142-L154 (Fig. 3).

### Relaxation measurements—summary of MBP dynamics

To characterize rmMBP further under these conditions, the dynamics ( $R_1$ ,  $R_2$ , and NOE) of the polypeptide backbone were recorded (Fig. 4 and Table 1) (47,60,61). Since rmMBP dissolved in 30% TFE- $d_2$  has a higher degree of stabilized structure than in 100 mM KCl, as indicated by CSI and SSP analysis, the following analysis further contrasts these differences and highlights this protein's extreme conformational dependence on environment.

#### rmMBP in 30% TFE- $d_2$

The  $R_1$  (spin-lattice relaxation) measurements indicate a relatively flat line with an average of  $\sim 1.64 \pm 0.23 \text{ s}^{-1}$  (Fig. 4 A).

There is a local minimum that is observed for the region bounded by residues P98-K102 (murine numbering). The relative errors observed for the  $R_1$  measurements may be due to slight temperature variations which may have caused minor peak-intensity fluctuations (96). Although rmMBP forms stabilized  $\alpha$ -helices under these conditions (discussed below), there is still expected to be a considerable amount of conformational plasticity in the protein. Particularly, tertiary conformational fluctuations may also introduce uncertainty in the measured relaxation rates. Hydrodynamic methods (e.g., small-angle x-ray scattering or pulsed field gradient nuclear magnetic resonance (48,50,97)), or long-range structural information (obtained via paramagnetic relaxation enhancement and SDSL (48)) would be helpful to provide further insight to the conformational behavior of rmMBP. The  $R_2$  (spin-spin relaxation) measurements fluctuate with local maxima (Fig. 4 C) that correspond to the SSP- and CSI-predicted  $\alpha$ -helices (Fig. 3, A and B, respectively), suggesting a higher degree of immobilization in those regions. There are four major regions of positive and large NOE intensities (Fig. 4 E) that correlate with the  $R_2$  data, and that correspond to the SSP and CSI plots that in-

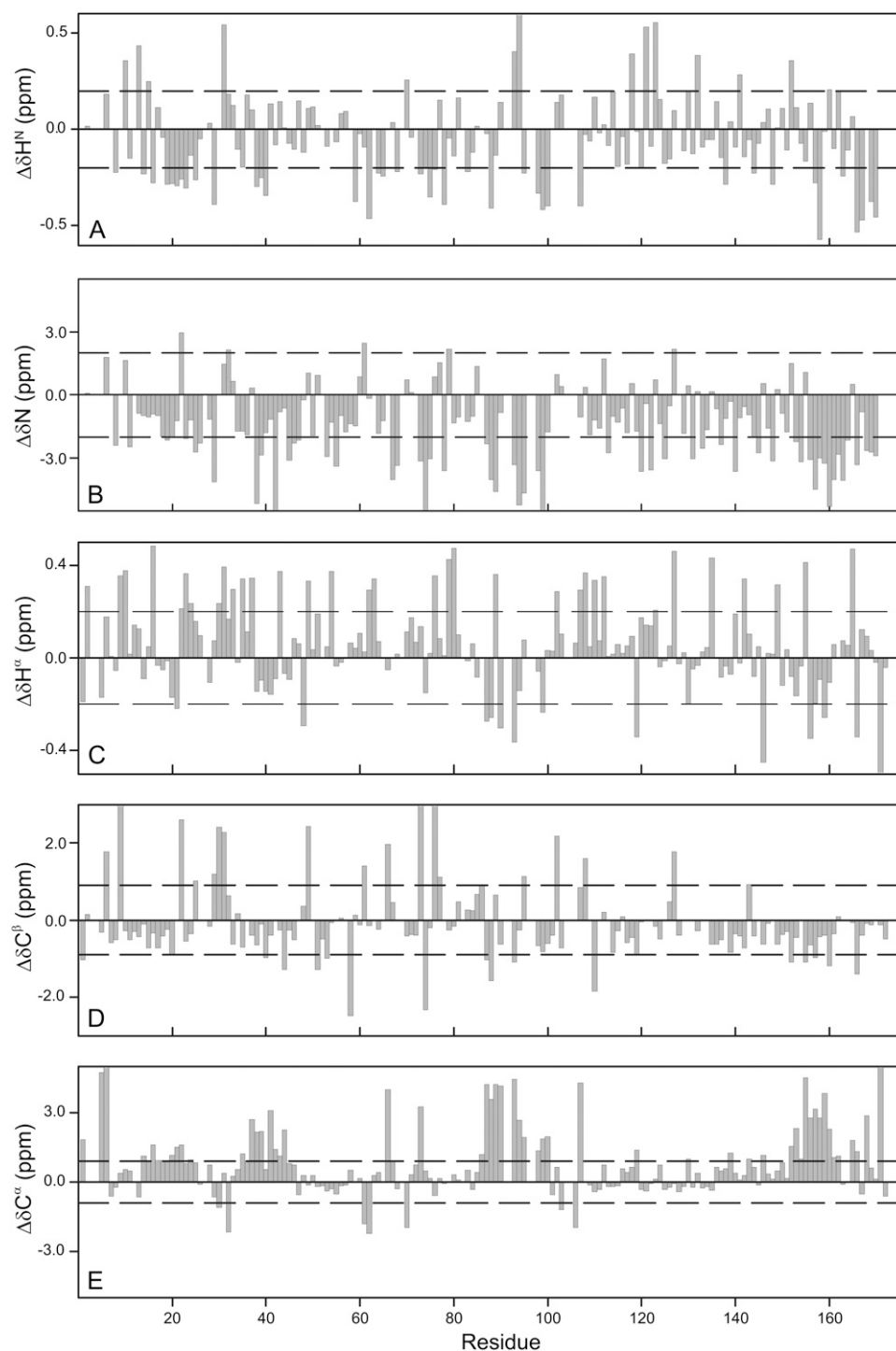


FIGURE 2 Chemical shift difference plots (A)  $H^N$ , (B) N, (C)  $H^\alpha$ , (D)  $C^\beta$ , (E)  $C^\alpha$ , for mmMBP in 30% TFE- $d_2$  at 300 K. The random coil values for  $H^N$ , N,  $H^\alpha$ , and  $C^\alpha$  have been adjusted for sequence dependence as previously described for the Golli-MBP isoform mmBG21 (64). The dashed lines in all the panels indicate the minimum threshold values for the formation of secondary structure elements. Generally, a consecutive stretch of four residues above the threshold value, or three residues below the threshold value, is considered to be an  $\alpha$ -helical or  $\beta$ -strand element, respectively.

indicate  $\alpha$ -helical propensity (Fig. 4 C, and Fig. 3, A, and B, respectively). We interpret these correlations as evidence that there are four TFE-stabilized  $\alpha$ -helices present in 18.5 kDa mmMBP. These  $\alpha$ -helices occur in regions that have been predicted to be structured via secondary structure prediction algorithms and PONDR analysis. There seems to be an area of higher restraint (possibly a less-stabilized helix than the other regions at L13-H21; dynamics identify mo-

tional restriction in this area, but the CSI does not quite meet the threshold for  $\alpha$ -helical structure). A final region of restraint is adjacent to the C-terminal helix, covering residues R157-R167. Although the CSI again does not quite meet the threshold for  $\alpha$ -helical structure (this region contains a prolyl residue and has an adjacent GG pair), one cannot rule out the influence of the C-terminal Leu-Glu-His<sub>6</sub>-tag on the stability of this region.



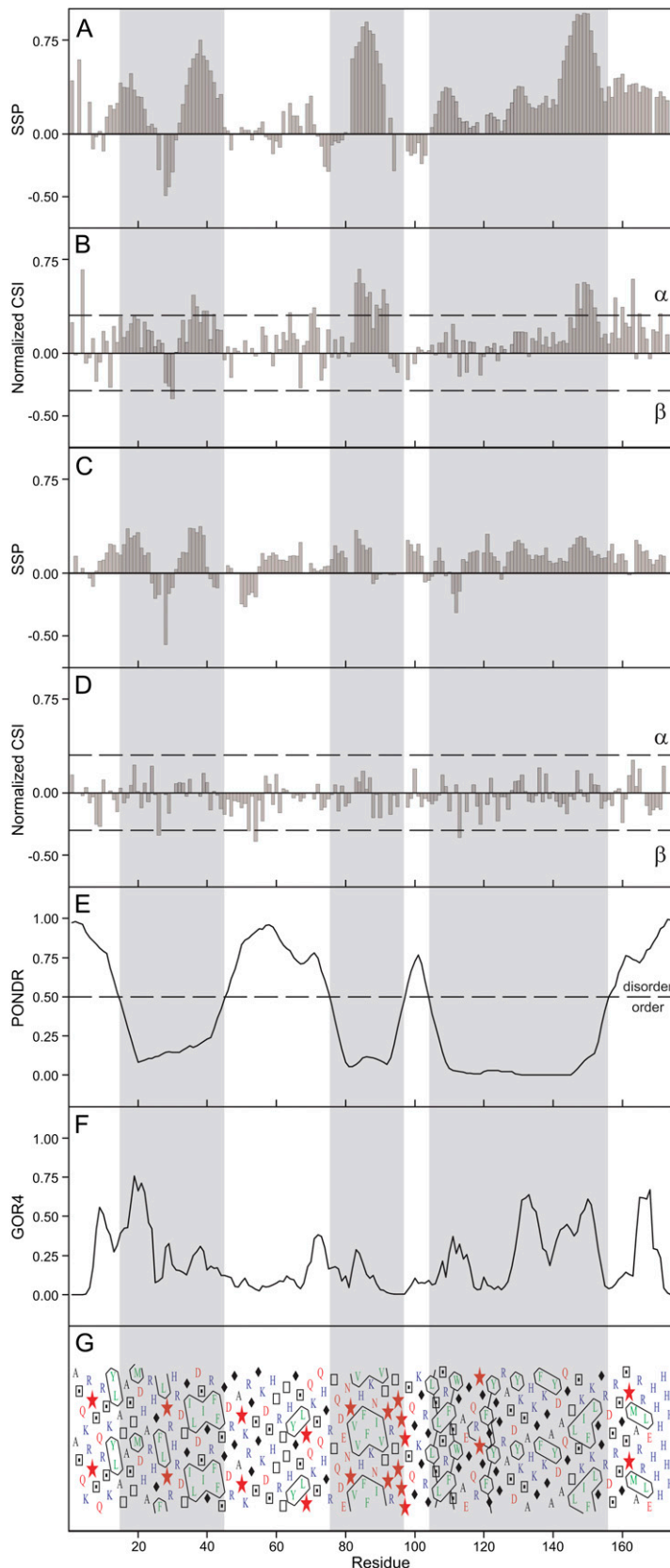


FIGURE 3 Experimentally measured parameters (SSP and normalized CSI) for (A and B) mmBP in 30% TFE- $d_2$  at 300 K, and (C and D) mmBP in 100 mM KCl at 277 K, for comparison with (E) IDP order predictions using PONDR (VL-XT Predictor) (92,93), (F) secondary structure predictions using GOR4 (94), and (G) a visually enhanced sequence representation using hydrophobic cluster analysis (HCA) (95). The gray bars align the PONDR-predicted regions of order over all the panels. The dashed lines in panels B and D represent minimum threshold values for the formation of either  $\alpha$ -helices (positive values), or  $\beta$ -strands (negative values). PONDR uses a neural network to predict regions of order/disorder in IDPs; the dashed line (E) represents the order/disorder threshold. Based on this prediction, mmBP has three regions of order which align with the  $\alpha$ -helical prediction from GOR4 (F). Hydrophobic cluster analysis (HCA) visually enhances primary sequence data using symbols ( $\square$ , T;  $\square$ , S;  $\blacklozenge$ , G;  $\blackstar$ , P), and colors (red, P and acidic residues D, E, N, Q; blue, basic residues H, K, R; green, hydrophobic residues V, L, I, F, W, M, Y; and black for all other residues, G, S, T, C, A). The hydrophobic clusters in mmBP (G) align with both the predicted  $\alpha$ -helices (F) and the experimentally measured  $\alpha$ -helices (A and B), and occur within the PONDR-predicted ordered regions (E).

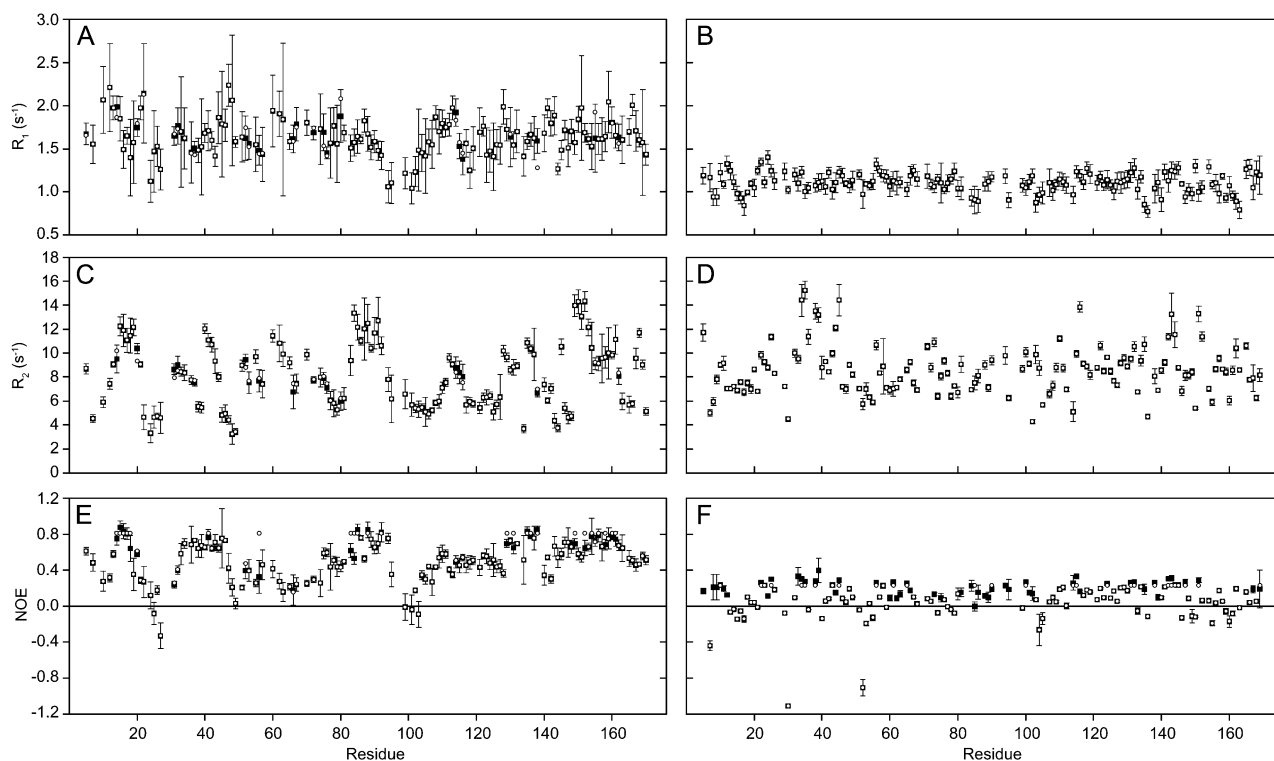


FIGURE 4 Relaxation measurements for rmMBP at 600 MHz and 300 K. We show the  $R_1$  values (A and B),  $R_2$  values (C and D), and  $\{^1\text{H}\}$ - $^{15}\text{N}$  NOE intensities (E and F) of  $^{13}\text{C}^{15}\text{N}$ -rmMBP in 30% TFE- $\text{d}_2$  (A, C, and E), and in 100 mM KCl (B, D, and F). Experimental values are shown as solid squares (■) with experimental error. The MODELFREE (v. 4.20) best fits are represented with open circles (○). The goodness of fit is clear at points where an open circle obscures the solid square.

#### rmMBP in 100 mM KCl

The  $R_1$  measurements form a relatively featureless line with an average  $R_1$  value of  $1.10 \pm 0.10 \text{ s}^{-1}$  (Fig. 4 B). The  $R_2$  measurements (Fig. 4 D) feature several regions (broadly, these are T33-D46 and T147-L154) of restricted motions that lie within the PONDR-predicted regions of order (Fig. 3 E), yet the corresponding NOE intensities (Fig. 4 F) are close to zero. This result indicates that there are no stabilized secondary structure elements in these regions, in contrast to the observations of  $\alpha$ -helices in the membrane-mimetic condition. The restrained motions in these two regions may be due to local hydrophobic collapse, since the HCA analysis identifies clusters of F, I, and L residues (Fig. 3 G). Interestingly, the immunodominant epitope (P82-P93) does not exhibit higher  $R_2$  values, and the NOE data are similar in intensity to the rest of the protein in that region (Fig. 4 F), suggesting that the  $\alpha$ -helix in this segment is disrupted under

these conditions. This result is consistent with previous observations of an 18-residue peptide fragment encompassing this region, that 100 mM KCl was insufficient to stabilize the amphipathic  $\alpha$ -helix fully (53). Overall, the NOE measurements do not suggest that there are any regions of restrained motions under these conditions, from which we conclude that rmMBP remains in a primarily random structural ensemble, even though there are segments that show a propensity toward secondary structure formation (Fig. 3). The overall degree of flexibility for this classic 18.5 kDa MBP isoform in aqueous solution is still not as extreme as for the early developmental Golli-MBP isoform rmBG21 (64). These two isoforms share a common segment of 56 amino acids, over which the NOE values show a good correlation and the  $R_1$  values a similar pattern (Data S1, Fig. S2), although the comparisons should be viewed with a degree of caution due to potential minor variations in experimental parameters.

**TABLE 1** Summary of the averaged relaxation ( $R_1$ ,  $R_2$ , and NOE) and order parameters ( $S^2$  and  $R_{\text{ex}}$ ) for rmMBP in either 30% TFE- $\text{d}_2$  or 100 mM KCl, at 300 K and at a magnetic field strength of 14.1 T (corresponding to the resonance frequency of 600.13 MHz for  $^1\text{H}$ )

Condition	$\tau_r$ (ns)	$S^2$	$R_{\text{ex}}$ ( $\text{s}^{-1}$ )	$R_1$ ( $\text{s}^{-1}$ )	$R_2$ ( $\text{s}^{-1}$ )	NOE
30% TFE- $\text{d}_2$	$6.74 \pm 0.09$	$0.63 \pm 0.11$	$1.17 \pm 0.66$	$1.64 \pm 0.23$	$8.07 \pm 0.73$	$0.51 \pm 0.08$
100 mM KCl	$1.26 \pm 0.01$	$0.46 \pm 0.04$	$7.17 \pm 0.41$	$1.10 \pm 0.10$	$8.57 \pm 0.37$	$0.09 \pm 0.01$



### Spectral density function analysis

In addition to the dynamics information obtained by measuring  $R_1$ ,  $R_2$ , and NOE intensities, spectral density mapping is useful to gauge motions in a qualitative manner, without introducing model-related systematic errors (48,98). The spectral density sampled at low frequency,  $J(0)$ , is used to identify slow (ms- $\mu$ s) internal motions. The value of the high frequency spectral density function  $J(\omega_H)$  is sensitive only to fast internal motions, reporting on the sub-nanosecond timescale. These fast motions make the value of  $J(\omega_H)$  larger than the average value. The spectral density function values derived for rmMBP at three frequencies are shown in Fig. 5 (A, C, and E: 30% TFE- $d_2$ ; B, D, and F: 100 mM KCl).

The higher frequency spectral density function values  $J(\omega_H)$  and  $J(\omega_N)$  are shown in Fig. 5, A–D. In Fig. 5 A (rmMBP in 30% TFE- $d_2$ ), the regions that display  $J(\omega_H)$  values below the average for the whole protein correspond to the segments L13-H21, T33-D46, V83-T92, and T142-L154, suggesting that these regions are under more restraint than the regions that have values higher than average. Furthermore, the identified regions correspond to  $J(0)$  values (Fig. 5 E) that are above the average values, again suggesting restricted motions indicative of secondary structure formation. The corresponding plot of  $J(\omega_H)$  values for rmMBP in 100 mM KCl (Fig. 5 B) is a relatively featureless curve, with no indication of either very fast or slow motions relative to the

average spectral density. It is interesting to note that the average values of  $J(\omega_H)$  are the same for rmMBP dissolved in both 30% TFE- $d_2$  or 100 mM KCl, although there are no indications of local restricted motion on the fast timescale under the latter condition.

There seems to be an indication of slight motional restriction of segments T33-D46 and Y142-L154 under the KCl conditions, as indicated by higher than average values observed for  $J(0)$  (Fig. 5 F) in these segments. This result may be indicative of the propensity of these regions to become structured upon encountering stabilizing conditions, such as membrane or protein interactions, or the result of local hydrophobic clustering (Fig. 3 G). The value of  $J(\omega_N)$  is much less informative in terms of backbone motion, although there is a local minimum observed for residues R94-Q100 for the protein in 30% TFE- $d_2$  (Fig. 5 C). This region encompasses a proline-rich segment which may form a polyproline type II helix (12,99) (see below). The corresponding  $J(\omega_N)$  plot for rmMBP in 100 mM KCl (Fig. 5 D) shows a featureless line. The spectral density function thus identifies regions that correspond with the stabilized secondary structural elements identified by CSI analysis (Fig. 3, A and B), the predicted  $\alpha$ -helices (Fig. 3 F), and the PONDR-predicted ordered segments (Fig. 3 E), and which encompass the hydrophobic clusters found in MBP (Fig. 3 G). These results clearly demonstrate the reliance of MBP on its surrounding

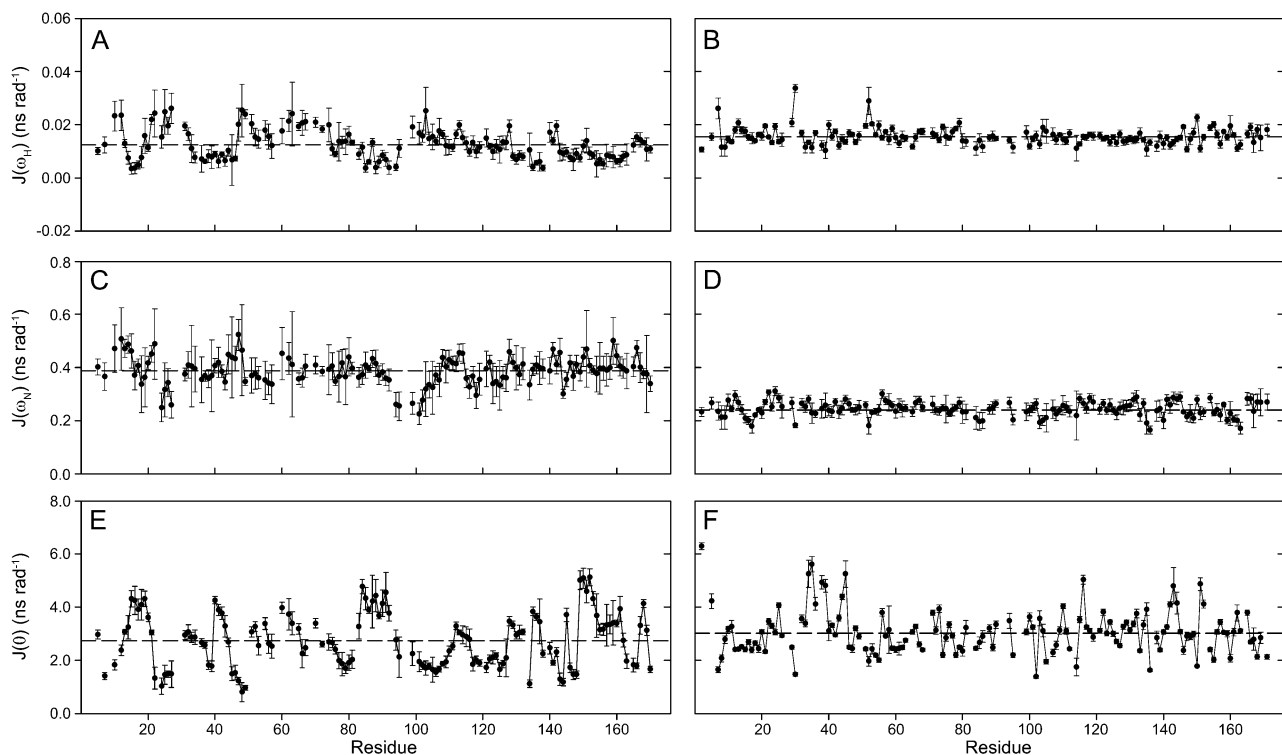


FIGURE 5 Spectral density function values for  $^{15}\text{N}$ -rmMBP at 300 K in 30% TFE- $d_2$  (A, C, and E), or 100 mM KCl (B, D, and F). The spectral density function was derived at three frequencies, 600.13 MHz ( $\omega_H$ , A and B), 60.8 MHz ( $\omega_N$ , C and D), and 0 (E and F). The dashed line in each panel represents the mean value of the respective spectral density function.

environment for the formation and stabilization of structure (7), behavior entirely consistent with IDPs in general (48,50–52).

### Model-free analysis—order parameters

The order parameters for both the aqueous and membrane-mimetic conditions were extracted from the experimental data using MODELFREE analysis, and are plotted in Fig. 6, with a complete list of values given in Data S1, Tables S2 and S3. The rotational correlation times (Table 1) extracted for rmMBP in 30% TFE-d<sub>2</sub> ( $6.74 \pm 0.09$  ns) and 100 mM KCl ( $1.26 \pm 0.01$  ns) are a further indication of the influence of the environment on the protein's structure. In 30% TFE-d<sub>2</sub>, rmMBP behaves as a relatively compact molecule, although it may sample several different tertiary conformations as noted above. A value of  $1.26 \pm 0.01$  ns for  $\tau_r$  is very fast for a protein of this size (19,422 Da for rmMBP (100)), which suggests that rmMBP in 100 mM KCl is in a primarily extended state, particularly when contrasted with the membrane-mimetic condition. The value of  $S^2$  provides a measure of rapid internal motions relative to the overall rotational diffusion (Fig. 6, A and B), whereas  $R_{ex}$  accounts for the presence of low frequency motions (Fig. 6, C and D) (101). Significantly large values of  $R_{ex}$  identify residues that experience conformational or chemical exchange on a microsecond-to-millisecond timescale, rates at which events such as ligand-binding or dissociation, or conformational exchange, often occur (102). Here, in 30% TFE-d<sub>2</sub> (Fig. 6 C), there are three major segments of rmMBP with a nearly contiguous run of significantly higher values of  $R_{ex}$  ( $>1.5$  s<sup>-1</sup>): Y12-H21, V84-T95, and S149-L154. Again, the latter two segments

correspond with the ordered secondary structure regions indicated in Fig. 3, whereas the first one (Y12-H21) overlaps partly with them. The large  $R_{ex}$  values observed for 100 mM KCl, in conjunction with the featureless  $S^2$  curve suggest either a high degree of disorder, and/or a high degree of exchange consistent with an averaged structural ensemble, and are therefore not an adequate description of the complex motions exhibited by rmMBP in an aqueous environment (102,103). The values of  $S^2$  and  $R_{ex}$  plotted (Fig. 6, B and D, respectively) should not be viewed as an absolute description of the motions and exchange processes occurring under these conditions (100 mM KCl), but rather an indication of the extreme conformational flexibility displayed by rmMBP in an aqueous solution condition. A comparison between the order parameters for each condition reveals that rmMBP is highly dependent on its environment for the stabilization of secondary (and by extension, tertiary) structure. These conditions also indicate where and when the approximations used to derive Eqs. 5–7 may break down when these analyses are applied to IDPs.

### Interactions of 18.5 kDa MBP with Ca<sup>2+</sup>-calmodulin—background and rationale

The 18.5 kDa isoform of MBP has previously been demonstrated to interact with CaM in a Ca<sup>2+</sup>-dependent manner using a variety of techniques including intrinsic single Trp fluorescence spectroscopy (9,104,105), chemical cross-linking and gel-shift assays (106), and dynamic light scattering (9). The in vitro interaction was shown to be specific (i.e., Ca<sup>2+</sup>-dependent), and occur at a 1:1 MBP/CaM ratio under near physiological conditions (250 mM NaCl, 50 mM Tris,

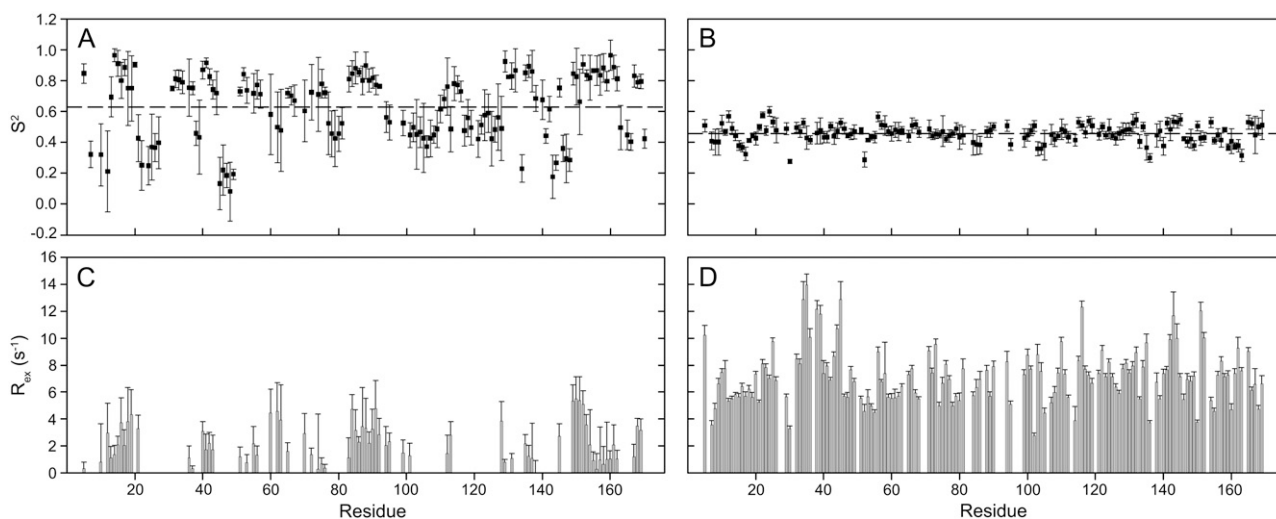


FIGURE 6 The MODELFREE-derived order parameters ( $S^2$  and  $R_{ex}$ ) for <sup>15</sup>N-rmMBP dissolved in 30% TFE-d<sub>2</sub> (panels A and C), and 100 mM KCl (panels B and D) at 300 K. The order parameters were determined using the globally optimized correlation times of  $6.74 \pm 0.09$  ns (30% TFE-d<sub>2</sub>, panels A and C), and  $1.26 \pm 0.01$  ns (100 mM KCl, panels B and D), from a Lipari-Szabo model-free analysis (76,77), with the extension of Cloue et al. (78), as described in the online MODELFREE manual (80). Errors were determined on the basis of 500 Monte Carlo simulations of Brent's implementation of Powell's method for multidimensional minimization (79,80). Complete values for each residue are provided for both conditions in Data S1, Tables S2 and S3.

pH 7.4, 10 mM CaCl<sub>2</sub>) with a dissociation constant of  $144 \pm 76$  nM (9). Subsequent proteomics analyses have revealed MBP to be one of many calmodulin-binding proteins in the brain (107,108), and MBP has recently been shown to function as an adaptor protein linking calmodulin to the BK<sub>Ca</sub> channel (11).

Our first prediction for the CaM-target was of a C-terminal segment on rmMBP (K132-R167), which was consistent with the experimental data (105,106). However, a C-terminal deletion mutant lacking this region also bound CaM specifically (104,109), and deiminated MBP (a reduced charge variant containing citrulline) bound CaM in a manner suggestive of a second binding site (9). We postulated that this putative second CaM-target could be the central immunodominant epitope (P82-P93) (53,54,86). Subsequent studies by us using SDSL/EPR showed that spin labels at all sites on 18.5 kDa rmMBP (i.e., multiple reporter sites compared to the single tryptophanyl residue) were immobilized upon the protein's association with CaM (10). We complemented these experimental studies by molecular modeling, using various peptide fragments of MBP (murine residues R41-R52, P82-P93, T147-D158), constructed in silico and modeled as  $\alpha$ -helices, and a collapsed form of CaM with both lobes clamping around the target. We observed from the docking simulations that the MBP peptides showed conformational variability and binding in various orientations, and that the balance of hydrophobic and electrostatic interactions determined the final binding mode. Moreover, the immunodominant epitope (P82-P93) was as plausible a CaM-target as the C-terminal segment (T147-D158) of rmMBP, when modeled as an  $\alpha$ -helix, but its interaction with CaM was energetically unfavorable when modeled as an extended strand (10). Thus, considering that there are at least two plausible CaM binding sites, NMR studies of the complex of CaM with full-length rmMBP were undertaken here with the goal of identifying definitively the primary CaM interaction site on MBP.

Uniformly-labeled <sup>13</sup>C<sup>15</sup>N-rmMBP associated with unlabeled CaM was used to record a series of three-dimensional spectra (CBCA(CO)NH, CBCANH, and HCC(CO)NH) to use with conventional protein backbone assignment methods. Sample preparation is noteworthy for the rmMBP-CaM complex, since it was very difficult to prepare a concentrated (0.6–1.0 mM) protein sample containing a minimal amount of stabilizing ions (maximum 100 mM), while limiting precipitation. (As described above for the free protein, aggregation was considered to be negligible on the basis of previous studies (9) and the quality and reproducibility of the HSQC spectra.) Furthermore, the resulting rmMBP-CaM complex was ~34 kDa, very close to the upper limit acceptable for solution NMR spectroscopy without employing specialized labeling techniques and pulse sequences (110). Thus, obtaining high-quality, usable NMR data from the rmMBP-CaM complex was extremely challenging and time-consuming. Titration of labeled rmMBP with unlabeled CaM

to facilitate assignments and monitor conformational changes was thus not attempted, although such an experimental strategy is possible with smaller systems (e.g., CaM and a peptide target, (88,111–113)). In all experiments here, in an attempt to circumvent a situation where both bound and unbound conformers coexist, the unlabeled binding partner was introduced into the system in molar excess of the labeled binding partner, to force the system equilibrium into the predominantly bound state (compare to (112)).

### Significant conformational changes of rmMBP upon association with CaM

The <sup>1</sup>H-<sup>15</sup>N HSQC of <sup>15</sup>N-labeled CaM interacting with unlabeled rmMBP is shown in Fig. 7; the <sup>1</sup>H-<sup>15</sup>N HSQC of <sup>15</sup>N-labeled rmMBP interacting with unlabeled CaM is shown in Fig. 8. The assignments of CaM (Fig. 7) are from previous work (114). Here, in addition, a total of 145 of the 164 expected H<sup>N</sup>-H correlations of rmMBP (Fig. 8) were assigned, and a further 20 C <sup>$\alpha$</sup>  and C <sup>$\beta$</sup>  resonances (176 and 152 expected, respectively) were identified from the CBCACONH and HCCCONH spectra; therefore, the backbone resonances of rmMBP bound to CaM were over 94% assigned.

The <sup>15</sup>N-CaM and unlabeled rmMBP showed chemical shift perturbations of the CaM resonances that were similar to what has been previously observed for CaM interacting with a binding partner (Fig. 7) (e.g., (111)). In the <sup>1</sup>H-<sup>15</sup>N HSQC of <sup>15</sup>N-rmMBP and unlabeled CaM (Fig. 8), many of the perturbed peaks of rmMBP mapped themselves to bulky hydrophobic residues (F, Y, and L), which may indicate exclusion of bulk solvent from the hydrophobic face, and/or a specific interaction. These results are consistent with the SDSL/EPR data showing greatest immobilization of the spin label at sites closest to small hydrophobic clusters on rmMBP (10). Although IDPs bind targets with high specificity, often involving multiple electrostatic interactions, the unbound portion of the polypeptide chain often retains considerable plasticity; thus, multiple hydrophobic interactions could be expected (33,42,43,115).

Using <sup>13</sup>C<sup>15</sup>N-rmMBP and unlabeled CaM, ~40 rmMBP resonances were observed shifted upfield in the <sup>1</sup>H dimension (7.0–8.2 ppm), and downfield in the <sup>15</sup>N dimension (123–133 ppm), relative to unbound rmMBP (Fig. 1). There was no change to the conformation of rmMBP upon the inclusion of 8 mM CaCl<sub>2</sub> to the rmMBP (sample 1, Materials and Methods), as judged by comparison of the peak positions of the pertinent HSQC spectra (results not shown). The <sup>1</sup>H-<sup>15</sup>N HSQC spectrum (Fig. 8) of rmMBP bound with CaM displays an increase in the overall dispersion of the peaks, and may indicate a more ordered state for rmMBP under these conditions. Moreover, these data are consistent with our previous results using SDSL/EPR which indicated that the entire rmMBP protein was involved in some interaction with CaM (10). The same extreme chemical shift perturbations are

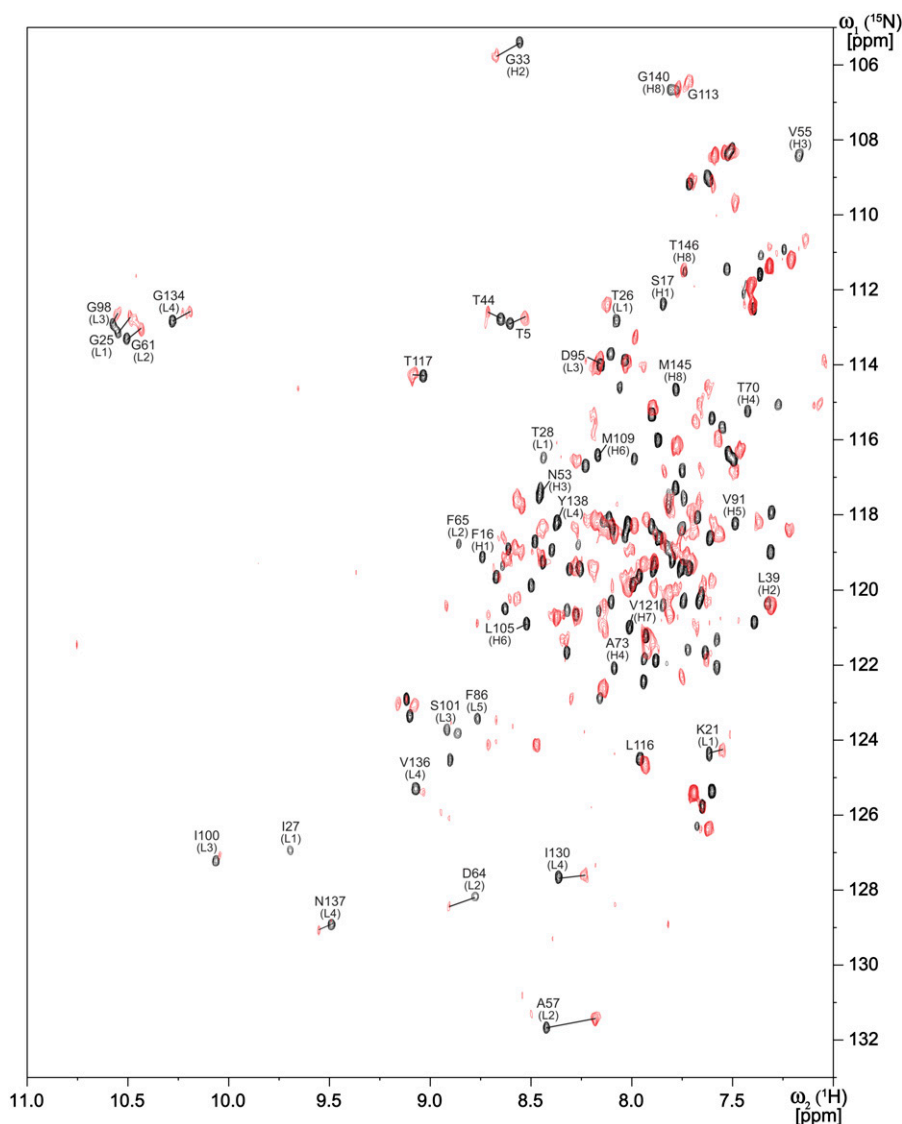


FIGURE 7 The  $^1\text{H}$ - $^{15}\text{N}$  HSQC spectra of uniformly  $^{15}\text{N}$ -labeled CaM (1.25 mM, *black contours*) and uniformly  $^{15}\text{N}$ -labeled CaM mixed with unlabeled rmMBP (0.64 mM CaM + 0.80 mM rmMBP, *red contours*). The resonance assignments shown are for unbound CaM and are from Ikura et al. (114); the labels shown correspond to the black (unbound) contours and indicate the secondary structure element ( $L$  = loop or  $H$  =  $\alpha$ -helix) with which each residue is associated. Crosspeaks that have obvious assignments are shown connected with black lines. Both spectra were recorded on samples in 100 mM KCl, 8 mM  $\text{CaCl}_2$ , pH 6.5, 10%  $\text{D}_2\text{O}$ , 0.75 mg DSS at 300 K.

not observed in the HSQC spectrum of CaM interacting with rmMBP (Fig. 7). Since there was a molar excess of rmMBP to force the equilibrium toward the bound state, we interpret this result to indicate that the structural perturbation of CaM is not as great as for rmMBP (Fig. 8) upon their association. The binding of CaM to rmMBP is  $\text{Ca}^{2+}$ -dependent, and here CaM is initially folded; but in the (open) halo-form, both the N- and C-terminal lobes of CaM appear to associate with rmMBP (Fig. 7), which is the most common mode of CaM binding. From these results, however, it is unclear whether CaM remains in its open form.

#### Identification of a C-terminal CaM-binding site on rmMBP

The C-terminal region of rmMBP (comprising roughly residues P120-R160) coincides with a cluster of highly perturbed  $\text{H}^{\text{N}}$ -N chemical shifts (Fig. 9). The combined weighted average chemical shift deviations for the  $\text{H}^{\text{N}}$  and

N shifts from random coil values for rmMBP alone at 277 K, alone at 300 K, and bound to CaM at 300 K, are shown, respectively, in Fig. 9, A–C. There is very little difference due to temperature on the observed  $\text{H}^{\text{N}}$  and N shifts of rmMBP alone (Fig. 9 D), but the addition of CaM has a large effect on these shifts (Fig. 9 E). This effect is also evident from the comparison of the HSQCs of unbound (Fig. 1) and CaM-bound (Fig. 8) rmMBP. Although the large  $\text{H}^{\text{N}}$ -N chemical shift deviations occur throughout the entire polypeptide chain, they are clustered in the C-terminal region. Furthermore, three glycyl residues (G155, G156, and G162) and a threonyl residue (T147) in this region have abnormally large  $\text{H}^{\text{N}}$  and N shift perturbations upon interaction with CaM (Fig. 8). Collectively, these observations are consistent with the premise that the C-terminus of posttranslationally unmodified 18.5 kDa rmMBP is the primary interaction site with CaM, as we have previously posited (9,104–106).

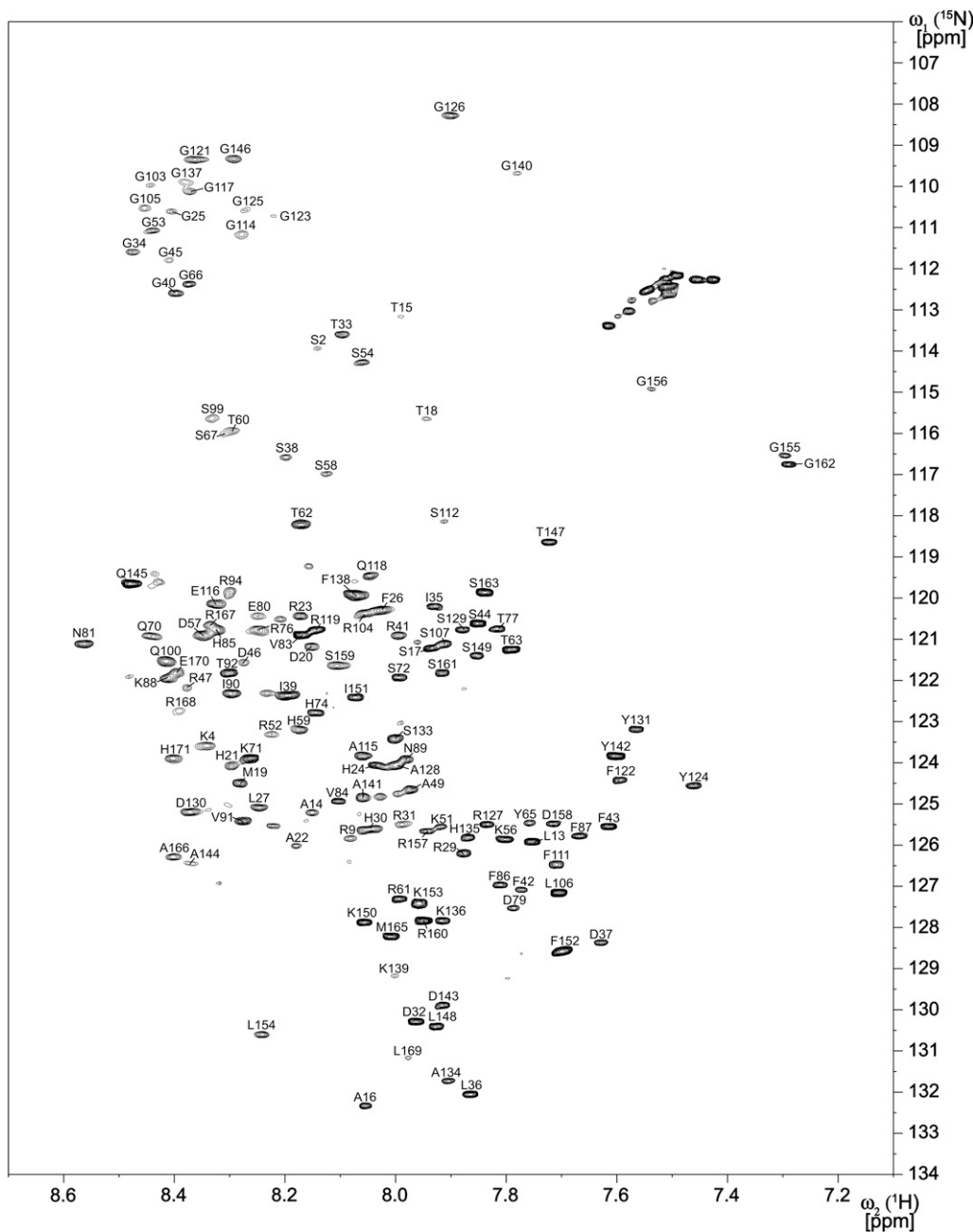


FIGURE 8 The  $^1\text{H}$ - $^{15}\text{N}$  HSQC spectrum of uniformly  $^{13}\text{C}^{15}\text{N}$ -labeled rmMBP bound with unlabeled CaM. The sample conditions were 100 mM KCl, 8 mM  $\text{CaCl}_2$ , pH 6.5, 10%  $\text{D}_2\text{O}$  at 300 K. The concentrations of the binding partners were 0.96 mM CaM and 0.78 mM  $^{13}\text{C}^{15}\text{N}$ -rmMBP. A total of 145 of 164 expected backbone peaks are assigned for rmMBP (there are 11 prolyl residues); peaks S10, G55, G75, and S109 are assigned, but appear below the displayed contour levels.

#### Local conformational changes in rmMBP upon CaM-binding

Recently, the hypothesis of coupled binding and folding has been explicitly stated for CaM and binding targets on IDPs (116). We now address the question of whether MBP gains ordered structure upon association with CaM. First of all, although the amphipathic  $\alpha$ -helix represents the well-studied, canonical CaM-target, it has become recognized that CaM-binding sites and modes of interaction are quite diverse (e.g.,

(117–120)). There is no strict requirement for the chemical shift perturbations observed in the  $^1\text{H}$ - $^{15}\text{N}$  HSQC to be indicative of an  $\alpha$ -helix, and the perturbations observed here (Fig. 8) may be representative of a different type of disorder-to-order transition characteristic of IDP binding (42).

Further evidence for this conjecture is based on SSP scores of rmMBP, calculated using only the  $\text{C}^\alpha$  and  $\text{C}^\beta$  chemical shifts, alone in 100 mM KCl at 277K (Fig. 10 A), and in

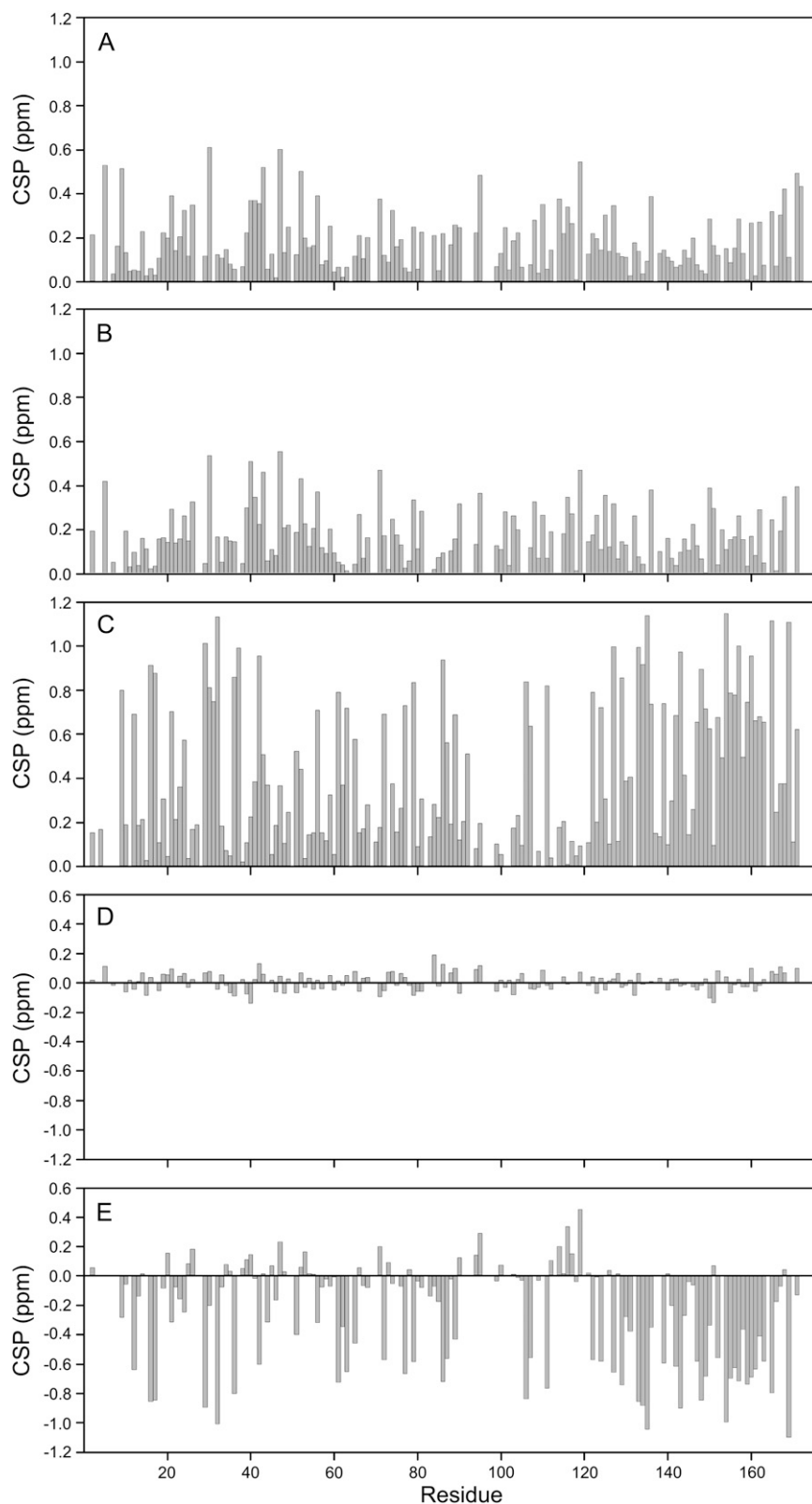


FIGURE 9 Chemical shift perturbation (CSP) plot of the weighted average of the  $H^N$  and  $N$  chemical shift deviations from random coil values. (A) rmMBP alone at 277 K; (B) rmMBP alone at 300 K; (C) rmMBP bound with CaM at 300 K; (D) difference between the CSP of rmMBP at 277 K and rmMBP recorded at 300 K; and (E) difference between the CSP of rmMBP at 277 K and rmMBP bound to CaM recorded at 300 K. The solute for all experiments was 100 mM KCl, pH 6.5, 10%  $D_2O$ , with 8 mM  $CaCl_2$  added to the CaM-containing samples. The weighted average of a specific residue was calculated as  $[(\Delta\delta H_N^2 + (\Delta\delta N^2/25))/2]^{1/2}$  (129).



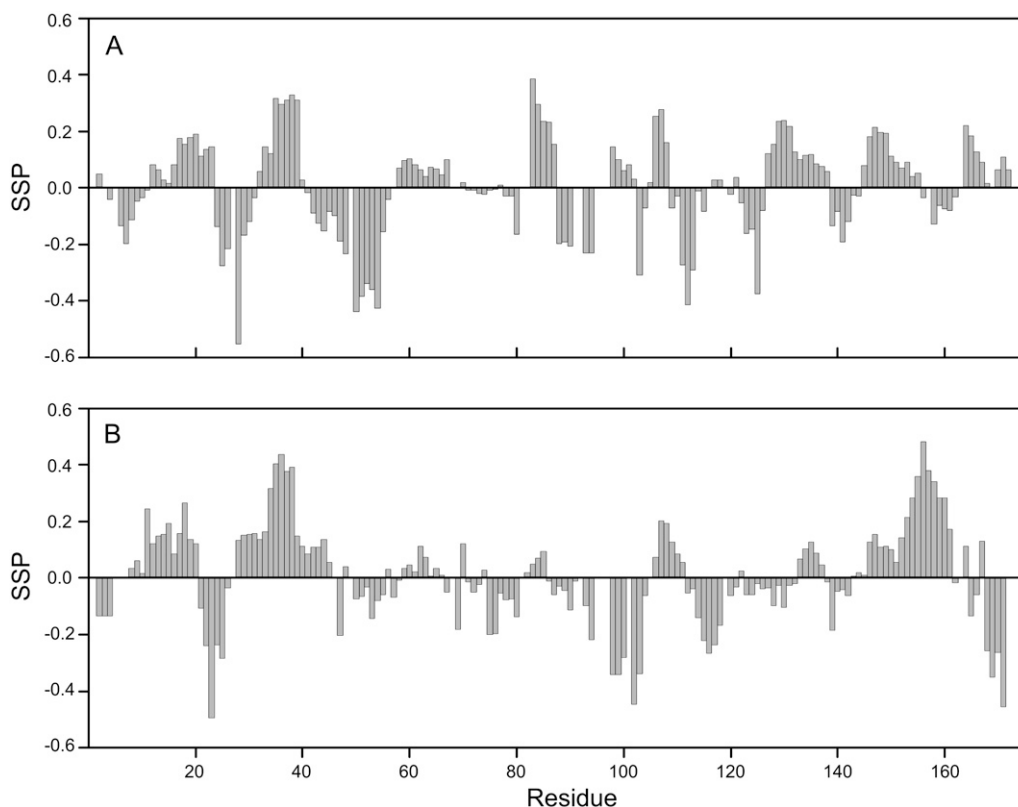


FIGURE 10 Comparison of the secondary structure propensity (SSP) of (A) rmMBP alone at 277 K, and (B) rmMBP bound with CaM at 300 K. Both samples were dissolved in 100 mM KCl, pH 6.5, 10% D<sub>2</sub>O, and 8 mM CaCl<sub>2</sub> was included with the CaM-containing sample. For both conditions, the SSP was calculated on the basis of the C<sup>α</sup> and C<sup>β</sup> shifts (in contrast to Fig. 3). The shifts were re-referenced as described by Marsh et al. (68) before the calculation of the SSP scores. The SSP score is interpreted as the percentage of conformers in the disordered ensemble that exhibit ordered secondary structure at a given residue (68).

association with CaM (Fig. 10 B). (The SSP scores presented in Fig. 3 were derived from the C<sup>α</sup>, C<sup>β</sup>, and H<sup>α</sup> chemical shifts, in contrast.) The SSP scores calculated from the C<sup>α</sup> and C<sup>β</sup> chemical shifts for rmMBP in 100 mM KCl at 277K (Fig. 10 A) show several regions of general order that correspond with the PONDR predictions (Fig. 3 E), although none of them could be categorized as a fully formed secondary structure element. This observation is consistent with the nature of IDP ensembles under nonstabilizing conditions. As a side note, the segments that show negative secondary structure propensities in Fig. 10 A (H24-D36, and R41-K56) are probably not  $\beta$ -strands, but rather polyproline type II helices (99), which have been demonstrated to be a common structural element of IDPs (see (12,121), and references therein). These two secondary structure types are indistinguishable based on chemical shift analysis alone, and other parameters such as coupling constants are required for their distinction (98,122,123). The existence of polyproline type II helices in MBP in these preparations is further supported by the fact that circular dichroism spectroscopy has shown minimal  $\beta$ -strand structure in 18.5 kDa MBP under similar conditions (124).

The SSP scores for rmMBP bound to CaM at 300 K are shown in Fig. 10 B. Chemical shifts in the N-terminal third of rmMBP show a pattern of order similar to that of unbound

rmMBP. The central immunodominant epitope (P82-P93) seems to be destabilized in the CaM-bound form of rmMBP relative to the free form, similar to what was observed in the relaxation measurements in 100 mM KCl (Fig. 4). Our previous molecular docking simulations indicated that an extended local conformation of this epitope would be unfavorable for CaM-binding (10). Our current data show that this central segment would not be a preferred CaM target for this highly-charged form of 18.5 kDa rmMBP (9,104). Furthermore, the C-terminal region shows a redistribution of the stabilized region, albeit within the PONDR-predicted ordered region. This observation suggests that the stabilization is coming from a different source (i.e., CaM) instead of the solvent or intrachain interactions. The residues from A144-S159 show a slightly increased propensity to form  $\alpha$ -helical structure in the CaM-bound rmMBP, compared to the unbound form.

If the CaM remains in an open conformation upon association with MBP (Fig. 7), then the interaction would appear to be noncanonical (119). As reviewed in the Introduction, transient  $\alpha$ -helices in IDPs are a common recognition motif for other proteins, and the MoRF hypothesis is an attractive one (45,46), especially as the C-terminus of rmMBP (residues T142-L154) has a propensity toward  $\alpha$ -helicity (Figs. 3

and 10 B). However, we cannot conclude unequivocally that this secondary structure type is present in the CaM-associated form. There are other CaM-binding proteins that appear to have an extended conformation of binding site when complexed with CaM, e.g., myristoylated alanine-rich C kinase substrate (MARCKS) and MARCKS-related peptides, and caldesmon (117,119,125). Moreover, there are other examples of IDP-protein binding without a substantial increase in ordered structure in the IDP (126,127), and further studies are required. Collectively, our observations are consistent with the premise that the C-terminus of posttranslationally unmodified 18.5 kDa rmMBP is the primary (preferred) interaction site with CaM, as previously posited (9,104–106), but we cannot rule out the possibility that it may be a non-canonical (non- $\alpha$ -helical) target.

### Interactions of 18.5 kDa MBP with $\text{Ca}^{2+}$ -calmodulin—significance and future studies

Recently, Kim et al. (11) reported that MBP acts as an adaptor, linking CaM with the  $\text{BK}_{\text{Ca}}$  channel, which suggests that MBP possesses multiple, specific interaction sites. Every isoform of MBP can and does adopt multiple unique conformations based on the local environment, and combinatorial posttranslational modifications could themselves induce or stabilize protein-binding targets (12,40,44,128). Overall, the results presented here demonstrate the polymorphic nature of MBP as an IDP, and further our understanding of the multifunctional nature of this protein (42,43). Specifically, our previous molecular modeling studies of MBP-derived peptides and CaM indicated relatively minor effects on docked energy of posttranslational modifications on the MBP target (10). However, the assumption in those *in silico* docking studies was that the MBP-derived peptide was  $\alpha$ -helical, and the CaM was modeled in fully collapsed form. If the recognition site on MBP is noncanonical (10,119), and if the CaM remains in open form, as both are suggested by the current data, then the mode of MBP-CaM binding may be significantly influenced by phosphorylation or deimination events in the target region and beyond (7,116). The current data support the conjecture that rmMBP interacts with CaM primarily through an interaction of the C-terminal residues A144-S159, but are not sufficient to probe the atomic details of this binding. Thus, future studies (e.g.,  $^{15}\text{N}$ - $^{13}\text{C}$  edited NOE spectroscopy experiments) will be necessary to delineate further the details of CaM-binding to MBP.

### CONCLUSIONS

Conformational adaptability is an important property of intrinsically disordered proteins, and underscores the importance of comparative structural studies of members of this class of proteins. In aqueous solution, the classic 18.5 kDa isoform of MBP is primarily disordered, but has transient

$\alpha$ -helices that are stabilized by membrane-mimetic conditions. Here, solution NMR spectroscopy (chemical shift index analysis, secondary structure propensity, and relaxation measurements) have been used to define three major segments of MBP (T33-D46, V83-T92, T142-L154) that form transient  $\alpha$ -helices that could be stabilized by protein- or lipid-binding, and that match bioinformatics predictions of increased order. One of these segments (V83-T92) represents an important membrane contact point and serves as a functional immunodominant epitope in the human neurodegenerative disease multiple sclerosis. Another segment (T142-L154) has been identified as the primary calmodulin-binding site, although perhaps through a noncanonical mode of recognition.

### SUPPLEMENTARY MATERIAL

To view all of the supplemental files associated with this article, visit [www.biophysj.org](http://www.biophysj.org).

The authors are grateful to Dr. Mitsuru Ikura (Ontario Cancer Institute, Toronto) for the gift of the plasmid for recombinant *Xenopus laevis* CaM, Dr. Vladimir Bamm and Ms. Anna Stronks for assistance with protein purification, and to Ms. Valerie Robertson (Guelph NMR Center), Dr. Martine Monette (Bruker BioSpin Canada), and Mr. Mumdooh Ahmed and Dr. Vladimir Ladizhansky (Physics, Guelph) for many helpful discussions, advice, and support.

This work was supported by the Canadian Institutes of Health Research (operating grant No. MOP 74468), and the Natural Sciences and Engineering Research Council of Canada (operating grant No. RG121541). D.S.L. was the recipient of an Ontario Graduate Scholarship. The University of Guelph NMR Centre benefited from funding by the Canada Foundation for Innovation, and the Ontario Innovation Trust.

### REFERENCES

1. Pribyl, T. M., C. W. Campagnoni, K. Kampf, T. Kashima, V. W. Handley, J. McMahon, and A. T. Campagnoni. 1993. The human myelin basic protein gene is included within a 179-kilobase transcription unit: expression in the immune and central nervous systems. *Proc. Natl. Acad. Sci. USA.* 90:10695–10699.
2. Campagnoni, A. T., T. M. Pribyl, C. W. Campagnoni, K. Kampf, S. Amur-Umarjee, C. F. Landry, V. W. Handley, S. L. Newman, B. Garbay, and K. Kitamura. 1993. Structure and developmental regulation of Golli-mbp, a 105-kilobase gene that encompasses the myelin basic protein gene and is expressed in cells in the oligodendrocyte lineage in the brain. *J. Biol. Chem.* 268:4930–4938.
3. Boggs, J. M. 2006. Myelin basic protein: a multifunctional protein. *Cell. Mol. Life Sci.* 63:1945–1961.
4. Dyer, C. A. 1997. Myelin proteins as mediators of signal transduction. *In Cell Biology and Pathology of Myelin: Evolving Biological Concepts and Therapeutic Approaches.* B. H. J. Juurlink, R. M. Devon, J. R. Doucette, A. J. Nazarali, D. J. Schreyer, and V. M. K. Verge, editors. Plenum Press, New York.
5. Givogri, M. I., E. R. Bongarzone, and A. T. Campagnoni. 2000. New insights on the biology of myelin basic protein gene: the neural-immune connection. *J. Neurosci. Res.* 59:153–159.
6. Campagnoni, A. T., and R. P. Skoff. 2001. The pathobiology of myelin mutants reveals novel biological functions of the MBP and PLP genes. *Brain Pathol.* 11:74–91.

7. Harauz, G., N. Ishiyama, C. M. D. Hill, I. R. Bates, D. S. Libich, and C. Farès. 2004. Myelin basic protein-diverse conformational states of an intrinsically unstructured protein and its roles in myelin assembly and multiple sclerosis. *Micron*. 35:503–542.
8. Kim, J. K., F. G. Mastronardi, D. D. Wood, D. M. Lubman, R. Zand, and M. A. Moscarello. 2003. Multiple sclerosis: an important role for post-translational modifications of myelin basic protein in pathogenesis. *Mol. Cell. Proteomics*. 2:453–462.
9. Libich, D. S., C. M. D. Hill, I. R. Bates, F. R. Hallett, S. Armstrong, A. Siemiarczuk, and G. Harauz. 2003. Interaction of the 18.5-kDa isoform of myelin basic protein with Ca<sup>2+</sup>-calmodulin: effects of deimination assessed by Trp fluorescence spectroscopy, dynamic light scattering, and circular dichroism. *Protein Sci.* 12:1507–1521.
10. Polverini, E., J. M. Boggs, I. R. Bates, G. Harauz, and P. Cavatorta. 2004. Electron paramagnetic resonance spectroscopy and molecular modeling of the interaction of myelin basic protein (MBP) with calmodulin (CaM)-diversity and conformational adaptability of MBP CaM-targets. *J. Struct. Biol.* 148:353–369.
11. Kim, H., S. Jo, H. J. Song, Z. Y. Park, and C. S. Park. 2007. Myelin basic protein as a binding partner and calmodulin adaptor for the BK(Ca) channel. *Proteomics*. 7:2591–2602.
12. Polverini, E., G. Rangaraj, D. S. Libich, J. M. Boggs, and G. Harauz. 2008. Binding of the proline-rich segment of myelin basic protein to SH3-domains—spectroscopic, microarray, and modeling studies of ligand conformation and effects of post-translational modifications. *Biochemistry*. 47:267–282.
13. Hill, C. M. D., and G. Harauz. 2005. Charge effects modulate actin assembly by classic myelin basic protein isoforms. *Biochem. Biophys. Res. Commun.* 329:362–369.
14. Hill, C. M. D., D. S. Libich, and G. Harauz. 2005. Assembly of tubulin by classic myelin basic protein isoforms and regulation by post-translational modification. *Biochemistry*. 44:16672–16683.
15. Boggs, J. M., G. Rangaraj, C. M. D. Hill, I. R. Bates, Y. M. Heng, and G. Harauz. 2005. Effect of arginine loss in myelin basic protein, as occurs in its deiminated charge isoform, on mediation of actin polymerization and actin binding to a lipid membrane in vitro. *Biochemistry*. 44:3524–3534.
16. Boggs, J. M., G. Rangaraj, W. Gao, and Y. M. Heng. 2006. Effect of phosphorylation of myelin basic protein by MAPK on its interactions with actin and actin binding to a lipid membrane in vitro. *Biochemistry*. 45:391–401.
17. Galiano, M. R., A. Andrieux, J. C. Deloulme, C. Bosc, A. Schweitzer, D. Job, and M. E. Hallak. 2006. Myelin basic protein functions as a microtubule stabilizing protein in differentiated oligodendrocytes. *J. Neurosci. Res.* 84:534–541.
18. Mastronardi, F. G., and M. A. Moscarello. 2005. Molecules affecting myelin stability: a novel hypothesis regarding the pathogenesis of multiple sclerosis. *J. Neurosci. Res.* 80:301–308.
19. Harauz, G., and A. A. Musse. 2007. A tale of two citrullines—structural and functional aspects of myelin basic protein deimination in health and disease. *Neurochem. Res.* 32:137–158.
20. Musse, A. A., and G. Harauz. 2007. Molecular “negativity” may underlie multiple sclerosis: role of the myelin basic protein family in the pathogenesis of MS. *Int. Rev. Neurobiol.* 79:149–172.
21. Moscarello, M. A., F. G. Mastronardi, and D. D. Wood. 2007. The role of citrullinated proteins suggests a novel mechanism in the pathogenesis of multiple sclerosis. *Neurochem. Res.* 32:251–256.
22. Uversky, V. N., J. R. Gillespie, and A. L. Fink. 2000. Why are “natively unfolded” proteins unstructured under physiologic conditions? *Proteins*. 41:415–427.
23. Dunker, A. K., C. J. Brown, J. D. Lawson, L. M. Iakoucheva, and Z. Obradovic. 2002. Intrinsic disorder and protein function. *Biochemistry*. 41:6573–6582.
24. Dyson, H. J., and P. E. Wright. 2006. According to current textbooks, a well-defined three-dimensional structure is a prerequisite for the function of a protein. Is this correct? *IUBMB Life*. 58:107–109.
25. Xie, H., S. Vucetic, L. M. Iakoucheva, C. J. Oldfield, A. K. Dunker, V. N. Uversky, and Z. Obradovic. 2007. Functional anthology of intrinsic disorder. 1. Biological processes and functions of proteins with long disordered regions. *J. Proteome Res.* 6:1882–1898.
26. Vucetic, S., H. Xie, L. M. Iakoucheva, C. J. Oldfield, A. K. Dunker, Z. Obradovic, and V. N. Uversky. 2007. Functional anthology of intrinsic disorder. 2. Cellular components, domains, technical terms, developmental processes, and coding sequence diversities correlated with long disordered regions. *J. Proteome Res.* 6:1899–1916.
27. Xie, H., S. Vucetic, L. M. Iakoucheva, C. J. Oldfield, A. K. Dunker, Z. Obradovic, and V. N. Uversky. 2007. Functional anthology of intrinsic disorder. 3. Ligands, post-translational modifications, and diseases associated with intrinsically disordered proteins. *J. Proteome Res.* 6:1917–1932.
28. Uversky, V. N., C. J. Oldfield, and A. K. Dunker. 2005. Showing your ID: intrinsic disorder as an ID for recognition, regulation and cell signaling. *J. Mol. Recognit.* 18:343–384.
29. Dosztanyi, Z., J. Chen, A. K. Dunker, I. Simon, and P. Tompa. 2006. Disorder and sequence repeats in hub proteins and their implications for network evolution. *J. Proteome Res.* 5:2985–2995.
30. Patil, A., and H. Nakamura. 2006. Disordered domains and high surface charge confer hubs with the ability to interact with multiple proteins in interaction networks. *FEBS Lett.* 580:2041–2045.
31. Bhalla, J., G. B. Storch, C. M. MacCarthy, V. N. Uversky, and O. Tcherkasskaya. 2006. Local flexibility in molecular function paradigm. *Mol. Cell. Proteomics*. 5:1212–1223.
32. Dyson, H. J., and P. E. Wright. 2002. Coupling of folding and binding for unstructured proteins. *Curr. Opin. Struct. Biol.* 12:54–60.
33. Fuxreiter, M., I. Simon, P. Friedrich, and P. Tompa. 2004. Prefolded structural elements feature in partner recognition by intrinsically unstructured proteins. *J. Mol. Biol.* 338:1015–1026.
34. Chi, S. W., S. H. Lee, D. H. Kim, M. J. Ahn, J. S. Kim, J. Y. Woo, T. Torizawa, M. Kainosho, and K. H. Han. 2005. Structural details on mdm2-p53 interaction. *J. Biol. Chem.* 280:38795–38802.
35. Eliezer, D., P. Barre, M. Kobaslija, D. Chan, X. Li, and L. Heend. 2005. Residual structure in the repeat domain of tau: echoes of microtubule binding and paired helical filament formation. *Biochemistry*. 44:1026–1036.
36. Oldfield, C. J., Y. Cheng, M. S. Cortese, P. Romero, V. N. Uversky, and A. K. Dunker. 2005. Coupled folding and binding with  $\alpha$ -helix-forming molecular recognition elements. *Biochemistry*. 44:12454–12470.
37. Tompa, P., C. Szasz, and L. Buday. 2005. Structural disorder throws new light on moonlighting. *Trends Biochem. Sci.* 30:484–489.
38. Tompa, P. 2005. The interplay between structure and function in intrinsically unstructured proteins. *FEBS Lett.* 579:3346–3354.
39. Vise, P. D., B. Baral, A. J. Latos, and G. W. Daughdrill. 2005. NMR chemical shift and relaxation measurements provide evidence for the coupled folding and binding of the p53 transactivation domain. *Nucleic Acids Res.* 33:2061–2077.
40. Solt, I., C. Magyar, I. Simon, P. Tompa, and M. Fuxreiter. 2006. Phosphorylation-induced transient intrinsic structure in the kinase-inducible domain of CREB facilitates its recognition by the KIX domain of CBP. *Proteins*. 64:749–757.
41. Sugase, K., H. J. Dyson, and P. E. Wright. 2007. Mechanism of coupled folding and binding of an intrinsically disordered protein. *Nature*. 447:1021–1025.
42. Fuxreiter, M., P. Tompa, and I. Simon. 2007. Local structural disorder imparts plasticity on linear motifs. *Bioinformatics*. 23:950–956.
43. Mészáros, B., P. Tompa, I. Simon, and Z. Dosztányi. 2007. Molecular principles of the interactions of disordered proteins. *J. Mol. Biol.* 372:549–561.
44. Baker, J. M., R. P. Hudson, V. Kanelis, W. Y. Choy, P. H. Thibodeau, P. J. Thomas, and J. D. Forman-Kay. 2007. CFTR regulatory region interacts with NBD1 predominantly via multiple transient helices. *Nat. Struct. Mol. Biol.* 14:738–745.

45. Vacic, V., C. J. Oldfield, A. Mohan, P. Radivojac, M. S. Cortese, V. N. Uversky, and A. K. Dunker. 2007. Characterization of molecular recognition features, MoRFs, and their binding partners. *J. Proteome Res.* 6:2351–2366.
46. Mohan, A., C. J. Oldfield, P. Radivojac, V. Vacic, M. S. Cortese, A. K. Dunker, and V. N. Uversky. 2006. Analysis of molecular recognition features (MoRFs). *J. Mol. Biol.* 362:1043–1059.
47. Dyson, H. J., and P. E. Wright. 2001. Nuclear magnetic resonance methods for elucidation of structure and dynamics in disordered states. *Methods Enzymol.* 339:258–270.
48. Dyson, H. J., and P. E. Wright. 2004. Unfolded proteins and protein folding studied by NMR. *Chem. Rev.* 104:3607–3622.
49. Dyson, H. J., and P. E. Wright. 2005. Elucidation of the protein folding landscape by NMR. *Methods Enzymol.* 394:299–321.
50. Receveur-Bréchet, V., J. M. Bourhis, V. N. Uversky, B. Canard, and S. Longhi. 2006. Assessing protein disorder and induced folding. *Proteins.* 62:24–45.
51. Radivojac, P., L. M. Iakoucheva, C. J. Oldfield, Z. Obradovic, V. N. Uversky, and A. K. Dunker. 2007. Intrinsic disorder and functional proteomics. *Biophys. J.* 92:1439–1456.
52. Mittag, T., and J. D. Forman-Kay. 2007. Atomic-level characterization of disordered protein ensembles. *Curr. Opin. Struct. Biol.* 17:3–14.
53. Farès, C., D. S. Libich, and G. Harauz. 2006. Solution NMR structure of an immunodominant epitope of myelin basic protein. Conformational dependence on environment of an intrinsically unstructured protein. *FEBS J.* 273:601–614.
54. Bates, I. R., J. B. Feix, J. M. Boggs, and G. Harauz. 2004. An immunodominant epitope of myelin basic protein is an amphipathic  $\alpha$ -helix. *J. Biol. Chem.* 279:5757–5764.
55. Libich, D. S., V. J. Robertson, M. M. Monette, and G. Harauz. 2004. Backbone resonance assignments of the 18.5 kDa isoform of murine myelin basic protein (MBP). *J. Biomol. NMR.* 29:545–546.
56. Libich, D. S., M. M. Monette, V. J. Robertson, and G. Harauz. 2007. NMR assignment of an intrinsically disordered protein under physiological conditions: the 18.5 kDa isoform of myelin basic protein. *Biomol. NMR Assign.* 1:61–63.
57. Spera, S., and A. Bax. 1991. Empirical correlation between protein backbone conformation and C- $\alpha$  and C- $\beta$  C-13 nuclear magnetic resonance chemical shifts. *J. Am. Chem. Soc.* 113:5490–5492.
58. Wishart, D. S., and B. D. Sykes. 1994. Chemical shifts as a tool for structure determination. *Methods Enzymol.* 239:363–392.
59. Wishart, D. S., and A. M. Nip. 1998. Protein chemical shift analysis: a practical guide. *Biochem. Cell Biol.* 76:153–163.
60. Lipari, G., A. Szabo, and R. M. Levy. 1982. Protein dynamics and NMR relaxation—comparison of simulations with experiment. *Nature.* 300:197–198.
61. Shojania, S., and J. D. O’Neil. 2006. HIV-1 Tat is a natively unfolded protein: the solution conformation and dynamics of reduced HIV-1 Tat-(1–72) by NMR spectroscopy. *J. Biol. Chem.* 281:8347–8356.
62. Bates, I. R., D. S. Libich, D. D. Wood, M. A. Moscarello, and G. Harauz. 2002. An Arg/Lys  $\rightarrow$  Gln mutant of recombinant murine myelin basic protein as a mimic of the deaminated form implicated in multiple sclerosis. *Protein Expr. Purif.* 25:330–341.
63. Ikura, M., S. Spera, G. Barbato, L. E. Kay, M. Krinks, and A. Bax. 1991. Secondary structure and side-chain  $^1\text{H}$  and  $^{13}\text{C}$  resonance assignments of calmodulin in solution by heteronuclear multidimensional NMR spectroscopy. *Biochemistry.* 30:9216–9228.
64. Ahmed, M. A., V. V. Bamm, G. Harauz, and V. Ladizhansky. 2007. The BG21 isoform of Golli myelin basic protein is intrinsically disordered with a highly flexible amino-terminal domain. *Biochemistry.* 46:9700–9712.
65. Wang, Y., and O. Jardetzky. 2002. Probability-based protein secondary structure identification using combined NMR chemical-shift data. *Protein Sci.* 11:852–861.
66. Schwarzingler, S., G. J. Kroon, T. R. Foss, J. Chung, P. E. Wright, and H. J. Dyson. 2001. Sequence-dependent correction of random coil NMR chemical shifts. *J. Am. Chem. Soc.* 123:2970–2978.
67. Keller, R. 2007. The Computer-Aided Resonance Assignment Tutorial. Cantina-Verlag, Goldau, Switzerland.
68. Marsh, J. A., V. K. Singh, Z. Jia, and J. D. Forman-Kay. 2006. Sensitivity of secondary structure propensities to sequence differences between  $\alpha$ - and  $\gamma$ -synuclein: implications for fibrillation. *Protein Sci.* 15:2795–2804.
69. Palmer, A. G., N. J. Skelton, W. J. Chazin, P. E. Wright, and M. Rance. 1992. Suppression of the effects of cross-correlation between dipolar and anisotropic chemical-shift relaxation mechanisms in the measurement of spin-spin relaxation rates. *Mol. Phys.* 75:699–711.
70. Kay, L. E., D. A. Torchia, and A. Bax. 1989. Backbone dynamics of proteins as studied by  $^{15}\text{N}$  inverse detected heteronuclear NMR spectroscopy: application to staphylococcal nuclease. *Biochemistry.* 28:8972–8979.
71. Boyd, J., U. Hommel, and I. D. Campbell. 1990. Influence of cross-correlation between dipolar and anisotropic chemical shift relaxation mechanisms upon longitudinal relaxation rates of  $^{15}\text{N}$  in macromolecules. *Chem. Phys. Lett.* 175:477–482.
72. Meiboom, S., and D. Gill. 1958. Modified spin-echo for measuring nuclear relaxation times. *Rev. Sci. Instrum.* 29:688–691.
73. Abragam, A. 1961. Principles of Nuclear Magnetism. Clarendon Press, Oxford.
74. Cavanagh, J., W. J. Fairbrother, A. G. Palmer, and N. J. Skelton. 1996. Protein NMR Spectroscopy. Principles and Practice. Academic Press (Elsevier Science), San Diego, CA.
75. Farrow, N. A., O. Zhang, A. Szabo, D. A. Torchia, and L. E. Kay. 1995. Spectral density function mapping using  $^{15}\text{N}$  relaxation data exclusively. *J. Biomol. NMR.* 6:153–162.
76. Lipari, G., and A. Szabo. 1982. Model-free approach to the interpretation of nuclear magnetic resonance relaxation in macromolecules. 1. Theory and range of validity. *J. Am. Chem. Soc.* 104:4546–4559.
77. Lipari, G., and A. Szabo. 1982. Model-free approach to the interpretation of nuclear magnetic resonance relaxation in macromolecules. 2. Analysis of experimental results. *J. Am. Chem. Soc.* 104:4559–4570.
78. Clore, G. M., A. Szabo, A. Bax, L. E. Kay, P. C. Driscoll, and A. M. Gronenborn. 1990. Deviations from the simple 2-parameter model-free approach to the interpretation of N-15 nuclear magnetic relaxation of proteins. *J. Am. Chem. Soc.* 112:4989–4991.
79. Mandel, A. M., M. Akke, and A. G. Palmer III. 1995. Backbone dynamics of *Escherichia coli* ribonuclease HI: correlations with structure and function in an active enzyme. *J. Mol. Biol.* 246:144–163.
80. Palmer, A. G. 2007. Modelfree Manual. [http://cpmcnet.columbia.edu/dept/gsas/biochem/labs/palmer/software/modelfree\\_manual.pdf](http://cpmcnet.columbia.edu/dept/gsas/biochem/labs/palmer/software/modelfree_manual.pdf).
81. Sattler, M., J. Schleucher, and C. Griesinger. 1999. Heteronuclear multidimensional NMR experiments for the structure determination of proteins in solution employing pulsed field gradients. *Prog. Nucl. Magn. Reson. Spectrosc.* 34:93–158.
82. Markley, J. L., A. Bax, Y. Arata, C. W. Hilbers, R. Kaptein, B. D. Sykes, P. E. Wright, and K. Wüthrich. 1998. Recommendations for the presentation of NMR structures of proteins and nucleic acids—IUPAC-IUBMB-IUPAB Inter-Union Task Group on the standardization of data bases of protein and nucleic acid structures determined by NMR spectroscopy. *Eur. J. Biochem.* 256:1–15.
83. Buck, M. 1998. Trifluoroethanol and colleagues: cosolvents come of age. Recent studies with peptides and proteins. *Q. Rev. Biophys.* 31:297–355.
84. Roccatano, D., G. Colombo, M. Fiorini, and A. E. Mark. 2002. Mechanism by which 2,2,2-trifluoroethanol/water mixtures stabilize secondary-structure formation in peptides: a molecular dynamics study. *Proc. Natl. Acad. Sci. USA.* 99:12179–12184.
85. Povey, J. F., C. M. Smales, S. J. Hassard, and M. J. Howard. 2007. Comparison of the effects of 2,2,2-trifluoroethanol on peptide and protein structure and function. *J. Struct. Biol.* 157:329–338.

86. Musse, A. A., J. M. Boggs, and G. Harauz. 2006. Deimination of membrane-bound myelin basic protein in multiple sclerosis exposes an immunodominant epitope. *Proc. Natl. Acad. Sci. USA*. 103:4422–4427.
87. Otzen, D. E., P. Sehgal, and L. W. Nesgaard. 2007. Alternative membrane protein conformations in alcohols. *Biochemistry*. 46:4348–4359.
88. Ikura, M., G. M. Clore, A. M. Gronenborn, G. Zhu, C. B. Klee, and A. Bax. 1992. Solution structure of a calmodulin-target peptide complex by multidimensional NMR. *Science*. 256:632–638.
89. Jo, E., and J. M. Boggs. 1995. Aggregation of acidic lipid vesicles by myelin basic protein: dependence on potassium concentration. *Biochemistry*. 34:13705–13716.
90. Zhong, L., V. V. Bamm, M. A. Ahmed, G. Harauz, and V. Ladzhansky. 2007. Solid-state NMR spectroscopy of 18.5 kDa myelin basic protein reconstituted with lipid vesicles: spectroscopic characterization and spectral assignments of solvent-exposed protein fragments. *Biochim. Biophys. Acta (Biomembr.)*. 1768:3193–3205.
91. Bates, I. R., J. M. Boggs, J. B. Feix, and G. Harauz. 2003. Membrane-anchoring and charge effects in the interaction of myelin basic protein (MBP) with lipid bilayers studied by spin-labeling. *J. Biol. Chem.* 278:29041–29047.
92. Romero, P., Z. Obradovic, X. Li, E. C. Garner, C. J. Brown, and A. K. Dunker. 2001. Sequence complexity of disordered protein. *Proteins*. 42:38–48.
93. Li, X., P. Romero, M. Rani, A. K. Dunker, and Z. Obradovic. 1999. Predicting protein disorder for N-, C-, and internal regions. *Genome Inform. Ser. Workshop Genome Inform.* 10:30–40.
94. Garnier, J., J. F. Gibrat, and B. Robson. 1996. GOR method for predicting protein secondary structure from amino acid sequence. *Methods Enzymol.* 266:540–553.
95. Gaboriaud, C., V. Bissery, T. Benchetrit, and J. P. Mornon. 1987. Hydrophobic cluster analysis: an efficient new way to compare and analyze amino acid sequences. *FEBS Lett.* 224:149–155.
96. Rule, G. S., and T. K. Hitchens. 2006. Fundamentals of Protein NMR Spectroscopy. Springer, Dordrecht, The Netherlands.
97. Bernado, P., E. Mylonas, M. V. Petoukhov, M. Blackledge, and D. I. Svergun. 2007. Structural characterization of flexible proteins using small-angle x-ray scattering. *J. Am. Chem. Soc.* 129:5656–5664.
98. Dyson, H. J., and P. E. Wright. 2002. Insights into the structure and dynamics of unfolded proteins from nuclear magnetic resonance. *Adv. Protein Chem.* 62:311–340.
99. Rath, A., A. R. Davidson, and C. M. Deber. 2005. The structure of “unstructured” regions in peptides and proteins: role of the polyproline II helix in protein folding and recognition. *Biopolymers*. 80:179–185.
100. Bates, I. R., P. Matharu, N. Ishiyama, D. Rochon, D. D. Wood, E. Polverini, M. A. Moscarello, N. J. Viner, and G. Harauz. 2000. Characterization of a recombinant murine 18.5-kDa myelin basic protein. *Protein Expr. Purif.* 20:285–299.
101. Palmer III, A. G. 1997. Probing molecular motion by NMR. *Curr. Opin. Struct. Biol.* 7:732–737.
102. Mukherjee, M., K. Dutta, M. A. White, D. Cowburn, and R. O. Fox. 2006. NMR solution structure and backbone dynamics of domain III of the E protein of tick-borne *Langat flavivirus* suggests a potential site for molecular recognition. *Protein Sci.* 15:1342–1355.
103. Marsh, J. A., C. Neale, F. E. Jack, W. Y. Choy, A. Y. Lee, K. A. Crowhurst, and J. D. Forman-Kay. 2007. Improved structural characterizations of the drkN SH3 domain unfolded state suggest a compact ensemble with native-like and non-native structure. *J. Mol. Biol.* 367:1494–1510.
104. Libich, D. S., C. M. D. Hill, J. D. Haines, and G. Harauz. 2003. Myelin basic protein has multiple calmodulin-binding sites. *Biochem. Biophys. Res. Commun.* 308:313–319.
105. Libich, D. S., and G. Harauz. 2002. Interactions of the 18.5 kDa isoform of myelin basic protein with  $\text{Ca}^{2+}$ -calmodulin: in vitro studies using fluorescence microscopy and spectroscopy. *Biochem. Cell Biol.* 80:395–406.
106. Libich, D. S., and G. Harauz. 2002. Interactions of the 18.5 kDa isoform of myelin basic protein with  $\text{Ca}^{2+}$ -calmodulin—in vitro studies using gel shift assays. *Mol. Cell. Biochem.* 241:45–52.
107. Berggard, T., G. Arrigoni, O. Olsson, M. Fex, S. Linse, and P. James. 2006. 140 mouse brain proteins identified by  $\text{Ca}^{2+}$ -calmodulin affinity chromatography and tandem mass spectrometry. *J. Proteome Res.* 5:669–687.
108. Zhang, Z., A. K. Ottens, E. C. Golden, R. L. Hayes, and K. K. W. Wang. 2006. Using calmodulin-affinity capture to study the rat brain calmodulin proteome and its vulnerability to calpain and caspase proteolysis. *Calcium Binding Proteins*. 1:125–129.
109. Hill, C. M. D., J. D. Haines, C. E. Antler, I. R. Bates, D. S. Libich, and G. Harauz. 2003. Terminal deletion mutants of myelin basic protein: new insights into self-association and phospholipid interactions. *Micron*. 34:25–37.
110. Tugarinov, V., P. M. Hwang, and L. E. Kay. 2004. Nuclear magnetic resonance spectroscopy of high-molecular-weight proteins. *Annu. Rev. Biochem.* 73:107–146.
111. Hayashi, N., M. Matsubara, Y. Jinbo, K. Titani, Y. Izumi, and N. Matsushima. 2002. Nef of HIV-1 interacts directly with calcium-bound calmodulin. *Protein Sci.* 11:529–537.
112. Kranz, J. K., E. K. Lee, A. C. Nairn, and A. J. Wand. 2002. A direct test of the reductionist approach to structural studies of calmodulin activity: relevance of peptide models of target proteins. *J. Biol. Chem.* 277:16351–16354.
113. Turjanski, A. G., D. A. Estrin, R. E. Rosenstein, J. E. McCormick, S. R. Martin, A. Pastore, R. R. Biekofsky, and V. Martorana. 2004. NMR and molecular dynamics studies of the interaction of melatonin with calmodulin. *Protein Sci.* 13:2925–2938.
114. Ikura, M., L. E. Kay, and A. Bax. 1990. A novel approach for sequential assignment of  $^1\text{H}$ ,  $^{13}\text{C}$ , and  $^{15}\text{N}$  spectra of proteins: heteronuclear triple-resonance three-dimensional NMR spectroscopy. Application to calmodulin. *Biochemistry*. 29:4659–4667.
115. Borg, M., T. Mittag, T. Pawson, M. Tyers, J. D. Forman-Kay, and H. S. Chan. 2007. Polyelectrostatic interactions of disordered ligands suggest a physical basis for ultrasensitivity. *Proc. Natl. Acad. Sci. USA*. 104:9650–9655.
116. Radivojac, P., S. Vucetic, T. R. O’Connor, V. N. Uversky, Z. Obradovic, and A. K. Dunker. 2006. Calmodulin signaling: analysis and prediction of a disorder-dependent molecular recognition. *Proteins*. 63:398–410.
117. Porumb, T., A. Crivici, P. J. Blackshear, and M. Ikura. 1997. Calcium binding and conformational properties of calmodulin complexed with peptides derived from myristoylated alanine-rich C kinase substrate (MARCKS) and MARCKS-related protein (MRP). *Eur. Biophys. J.* 25:239–247.
118. Osawa, M., H. Tokumitsu, M. B. Swindells, H. Kurihara, M. Orita, T. Shibamura, T. Furuya, and M. Ikura. 1999. A novel target recognition revealed by calmodulin in complex with  $\text{Ca}^{2+}$ -calmodulin-dependent kinase kinase. *Nat. Struct. Biol.* 6:819–824.
119. Hoeflich, K. P., and M. Ikura. 2002. Calmodulin in action: diversity in target recognition and activation mechanisms. *Cell*. 108:739–742.
120. Ishida, H., and H. J. Vogel. 2006. Protein-peptide interaction studies demonstrate the versatility of calmodulin target protein binding. *Protein Pept. Lett.* 13:455–465.
121. Shi, Z., R. W. Woody, and N. R. Kallenbach. 2002. Is polyproline II a major backbone conformation in unfolded proteins? *Adv. Protein Chem.* 62:163–240.
122. Lam, S. L., and V. L. Hsu. 2003. NMR identification of left-handed polyproline type II helices. *Biopolymers*. 69:270–281.
123. Czinki, E., and A. G. Császár. 2007. Empirical isotropic chemical shift surfaces. *J. Biomol. NMR*. 38:269–287.
124. Polverini, E., A. Fasano, F. Zito, P. Riccio, and P. Cavatorta. 1999. Conformation of bovine myelin basic protein purified with bound lipids. *Eur. Biophys. J.* 28:351–355.

125. Permyakov, S. E., I. S. Millett, S. Doniach, E. A. Permyakov, and V. N. Uversky. 2003. Natively unfolded C-terminal domain of caldesmon remains substantially unstructured after the effective binding to calmodulin. *Proteins*. 53:855–862.
126. Bourhis, J. M., V. Receveur-Bréchet, M. Oglesbee, X. Zhang, M. Buccellato, H. Darbon, B. Canard, S. Finet, and S. Longhi. 2005. The intrinsically disordered C-terminal domain of the measles virus nucleoprotein interacts with the C-terminal domain of the phosphoprotein via two distinct sites and remains predominantly unfolded. *Protein Sci*. 14:1975–1992.
127. Sigalov, A. B., A. V. Zhuravleva, and V. Y. Orekhov. 2007. Binding of intrinsically disordered proteins is not necessarily accompanied by a structural transition to a folded form. *Biochimie*. 89:419–421.
128. Ramwani, J. J., R. M. Epand, and M. A. Moscarello. 1989. Secondary structure of charge isomers of myelin basic protein before and after phosphorylation. *Biochemistry*. 28:6538–6543.
129. Grzesiek, S., S. J. Stahl, P. T. Wingfield, and A. Bax. 1996. The CD4 determinant for downregulation by HIV-1 Nef directly binds to Nef. Mapping of the Nef binding surface by NMR. *Biochemistry*. 35:10256–10261.